J. Fluid Mech. (2019), *vol.* 863, *pp.* 1091–1122. © Cambridge University Press 2019. This is a work of the U.S. Government and is not subject to copyright protection in the United States.
doi:10.1017/jfm.2018.1029

Amplification and structure of streamwise-velocity fluctuations in compression-corner shock-wave/turbulent boundary-layer interactions

M. A. Mustafa[1], N. J. Parziale[1,†], M. S. Smith[2] and E. C. Marineau[2]

[1]Department of Mechanical Engineering, Stevens Institute of Technology, Hoboken, NJ 07030, USA

[2]Arnold Engineering Development Complex – White Oak, Silver Spring, MD 20903, USA

(Received 4 September 2018; revised 9 November 2018; accepted 13 December 2018; first published online 31 January 2019)

In this work, we study the effect of the compression-corner angle on the streamwise turbulent kinetic energy (sTKE) and structure in Mach 2.8 flow. Krypton tagging velocimetry (KTV) is used to investigate the incoming turbulent boundary layer and flow over 8°, 16°, 24° and 32° compression corners. The experiments were performed in a 99 % N_2 and 1 % Kr gas mixture in the Arnold Engineering Development Complex (AEDC) Mach 3 Calibration Tunnel (M3CT) at $Re_\Theta = 1750$. A figure of merit is defined as the wall-normal integrated sTKE ($\overline{\text{sTKE}}$), which is designed to identify turbulence amplification by accounting for the root-mean-squared (r.m.s.) velocity fluctuations and shear-layer width for the different geometries. We observe that the $\overline{\text{sTKE}}$ increases as an exponential with the compression-corner angle near the root when normalized by the boundary-layer value. Additionally, snapshot proper orthogonal decomposition (POD) is applied to the KTV results to investigate the structure of the flow. From the POD results, we extract the dominant flow structures and compare each case by presenting mean-velocity maps that correspond to the largest positive and negative POD mode coefficients. Finally, the POD spectrum reveals an inertial range common to the boundary-layer and each compression-corner flow that is present after the first ≈10 dominant POD modes.

Key words: high-speed flow, shock waves, turbulent boundary layers

1. Introduction

The interaction of shock waves and boundary layers is a fundamental problem in high-speed flow physics motivated by practical applications. Dolling (2001) states '(shock-wave boundary-layer interactions) are ubiquitous in high-speed flight, occurring in an almost limitless number of external and internal flow problems relevant to aircraft, missiles, rockets, and projectiles. Maximum mean and fluctuating pressure levels and thermal loads that a structure is exposed to are generally found in regions of shock/boundary-layer and shock/shear-layer interaction and can (affect) vehicle and

† Email address for correspondence: nick.parziale@gmail.com

https://doi.org/10.1017/jfm.2018.1029 Published online by Cambridge University Press

component geometry, structural integrity, material selection, fatigue life, the design of thermal protection systems, weight, and cost'. Consequently, to better design high-speed vehicles it is necessary to understand the fundamentals of this complex interaction. This ubiquity has led to a plethora of computational (Adams 2000; Wu & Martin 2007, 2008; John, Kulkarni & Natarajan 2014; Wang *et al.* 2015) and experimental (Settles, Vas & Bogdonoff 1976; Settles, Fitzpatrick & Bogdonoff 1979; Smits & Muck 1987; Humble, Scarano & van Oudheusden 2007; Humble *et al.* 2009; Giepman, Schrijer & van Oudheusden 2015) investigations into this interaction. Reviews (Settles 1994; Knight *et al.* 2003; Gaitonde 2015) highlight the current state of the research.

The breadth of interactions is vast, as discussed in the introductory chapters of Babinsky & Harvey (2011). In this work, we focus our study on the effect of the compression-corner angle on the streamwise turbulent kinetic energy (sTKE) and structure in Mach 2.8 flow. For example, this canonical flow may be observed in practice as the deflection of a control surface on a vehicle in high-speed flight or in the flow path of a high-speed, air-breathing engine. Trends of velocity-fluctuation amplitude and turbulence structure with compression-corner angle imply a change in the shear stress, heat-transfer rate and mixing properties of the flow, all of which have simulation and design implications.

An important feature of shock-wave/boundary-layer interaction (SWBLI) is the modification of turbulence stresses across the flow field. Experimental investigations have determined that there is significant amplification of turbulence across shocks. Smits & Muck (1987) studied the shock-wave/turbulent boundary-layer interaction over three compression corners and reported amplification factors of 4–15 for the mass-flux fluctuation intensity, and even larger factors for the shear stresses. Humble *et al.* (2007) used particle image velocimetry (PIV) to study the flow over a flat plate with an impinging shock and found amplification factors of the same order of magnitude as Smits & Muck (1987). Computational efforts have also provided similar insight. In the direct numerical simulation (DNS) of Wu & Martin (2007), amplification factors of 6–24 for the Reynolds stresses were calculated for a Mach 2.9 flow over a 24° compression ramp. Using large eddy simulation (LES), Porter & Poggie (2017) reported amplification factors of 2.3–7.6 for the Reynolds stresses for a Mach 2.25 flow over a 24° compression ramp.

Another important feature of turbulent flow is the existence of structures of various time and length scales (Tennekes & Lumley 1972). The interaction of this wide range of turbulent scales with a shock wave yields a rich, fundamental fluid-mechanics problem. Being able to quantify these scales and deepening our understanding of the physical properties and relative importance of these structures will further improve our ability to model turbulent flows. One analytical tool that accomplishes this is proper orthogonal decomposition (POD). It was first introduced to the fluid dynamics community by Lumley (Lumley 1967; Berkooz, Holmes & Lumley 1993) as a means to extract coherent structures from flow fields. A review of POD analysis in the broader context of modal analysis can be found in Taira *et al.* (2017). The fundamental idea of POD is to decompose the velocity field into a series of modes weighted based on the amount of kinetic energy they contain, each of which can be interpreted as a coherent structure. This technique has been used to study combustion engines (Druault, Guibert & Alizon 2005; Chen, Reuss & Sick 2012; Chen *et al.* 2013), turbulent flow over a fence (Orellano & Wengle 2001), open cavity flow (Murray, Sällström & Ukeiley 2009), axisymmetric jet flow and mixing layers (Bonnet *et al.* 1994) and the turbulent flow over a cylinder (Tu *et al.* 2014), to name a few.

https://doi.org/10.1017/jfm.2018.1029 Published online by Cambridge University Press

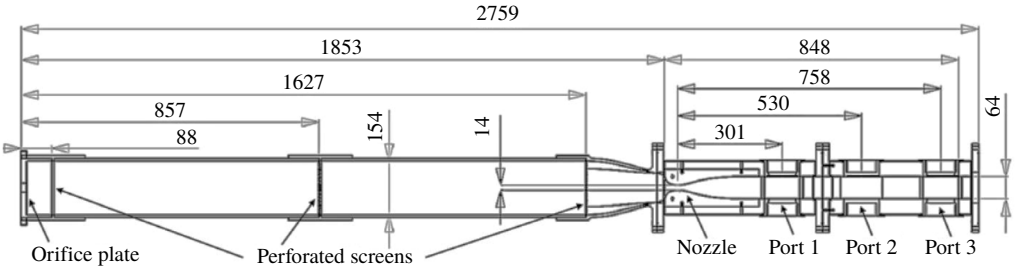


FIGURE 1. Sketch of AEDC Mach 3 Calibration Tunnel (M3CT). Dimensions in millimetres. The measurements are made at 'Port 2'.

There are not many applications of POD to SWBLIs in the literature. One example is that of Piponniau *et al.* (2012) where a POD analysis was performed on PIV results from an induced-shock-wave/turbulent boundary-layer interaction. The authors aimed to investigate 'the unsteady breathing of the recirculating bubble at low frequency and the Kelvin-Helmholtz instabilities developing at moderate frequency'.

We begin this paper by describing the experimental facility, the Mach 3 Calibration Tunnel (the M3CT) and the measurement technique, krypton tagging velocimetry (KTV). Then, we establish that the incoming flow is nominally a canonical supersonic, turbulent boundary layer over a flat plate by reporting KTV measurements of mean- and fluctuating-velocity profiles and comparing them to those found in the literature. We then report results of mean- and fluctuating-velocity profiles of flows over 8°, 16°, 24° and 32° compression corners which yields a case-wise comparison of streamwise turbulent kinetic energy (sTKE). Finally, we apply POD to the KTV results and discuss the eigenspectra and make case-wise comparisons of the most energetic POD modes.

2. Facility and experimental set-up

The experiments were performed in the Arnold Engineering Development Complex (AEDC) Mach 3 Calibration Tunnel (M3CT) in Silver Spring, MD (figure 1). The tunnel is comprised of a large vacuum tank attached to a converging diverging nozzle. An orifice plate was added upstream of the nozzle as in Zahradka *et al.* (2016*a*) and Mustafa *et al.* (2017*a*) to control the free-stream pressure. A flexible isolation bag was added upstream of the orifice to contain the 99 % N_2/1 % Kr gas mixture. The flexibility ensured that the bag stayed at the constant ambient pressure of the laboratory. A valve is cycled downstream of the nozzle to run the tunnel. The run condition calculations can be found in Zahradka *et al.* (2016*a*) and Mustafa *et al.* (2017*a*) (table 1).

To ensure that the M3CT started properly and to visualize the shock-wave/turbulent boundary-layer interaction structures, a Z-type schlieren set-up (Settles 2001) was used to visualize the flow field over the compression corners. The schlieren set-up consisted of a sparklamp light source and an Integrated Design Tools N3 camera recording at 100 frames-per-second with a 50 ns exposure time. The knife edge was set as a horizontal cutoff. Figure 2 shows the mean of 100 exposures of the schlieren visualization for each wedge with the mean shock position marked, as determined by local curve fitting to the image intensity. Approximately 900 snapshots of data were collected for each geometry, which corresponds to a physical time of 90 s.

https://doi.org/10.1017/jfm.2018.1029 Published online by Cambridge University Press

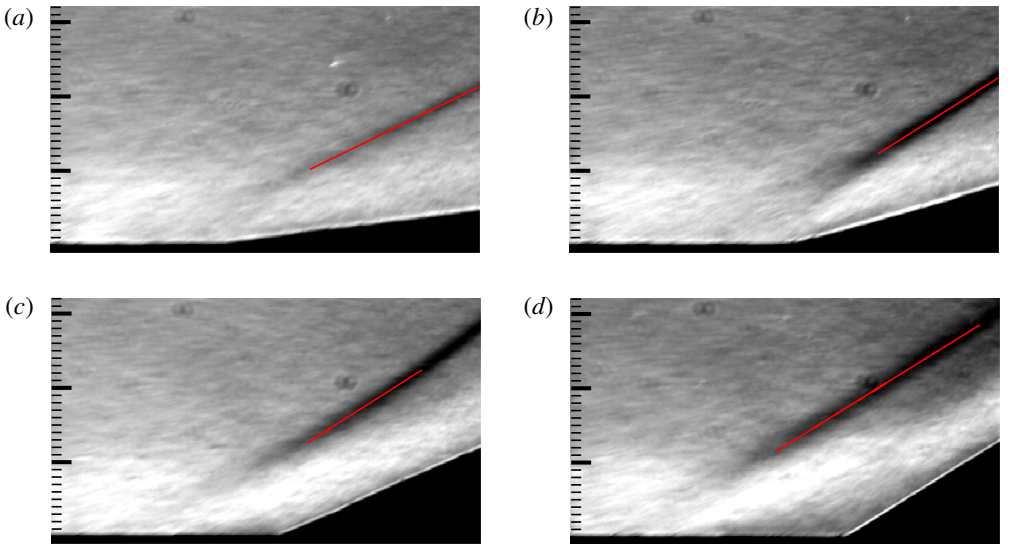


FIGURE 2. (Colour online) Mean schlieren images for the (*a*) 8°, (*b*) 16°, (*c*) 24° and (*d*) 32° corners, respectively. Flow is left to right. Major tick marks are at 10 mm. Incoming boundary-layer thickness is $\delta = 10.25$ mm. Mean shock position shown in red.

M_∞ (−)	P_∞ (Pa)	T_∞ (K)	ρ_∞ (kg m^{-3})	Re_∞^{unit} (1 m^{-1})	Re_Θ (−)	U_∞ (m s^{-1})	δ (mm)	u_τ (m s^{-1})	ν_w (m^2 s^{-1})	$\eta = \nu_w/u_\tau$ (μm)
2.77	1010	118	0.030	2.30×10^6	1750	612	10.25	34	0.0014	40

TABLE 1. Values of M_∞, P_∞, T_∞, ρ_∞, Re_∞^{unit}, Re_Θ, U_∞ and δ are the Mach number, pressure, temperature, density, unit Reynolds number, momentum-thickness Reynolds number, velocity and boundary-layer thickness for the AEDC M3CT tunnel with the 19.1 mm orifice plate. Additionally, u_τ, ν_w and η are the friction velocity, kinematic viscosity at the wall and the viscous length, respectively. Values reported here are for 'Port 2' in figure 1.

To compare the flow field investigated in the present work with that in the literature, the mean initial shock angles (β) are plotted in figure 3 against the wedge angle θ. The graph shows that for the 8° wedge, β is equal to the calculated value from inviscid theory. Beginning with the 16° wedge, β approaches a constant value of ≈32°. This trend of β approaching a constant value is in agreement with the work by Spaid & Frishett (1972), which was experimental work performed at Mach 2.9. The value of β for the 8° and 16° wedge is in agreement with previous work by Smits & Muck (1987). The initial shock angle for the 24° wedge is in agreement with DNS work by Wu & Martin (2007) and experimental work by Settles *et al.* (1976) and Mustafa *et al.* (2017*a*). From the comparison of the initial shock angle with those in the literature, we conclude that the flow has started and these geometries can be studied in the M3CT. In addition to shock angle, we show the extent of flow separation for each corner angle as a distribution of the instantaneous normalized velocity at the root (figure 11).

https://doi.org/10.1017/jfm.2018.1029 Published online by Cambridge University Press

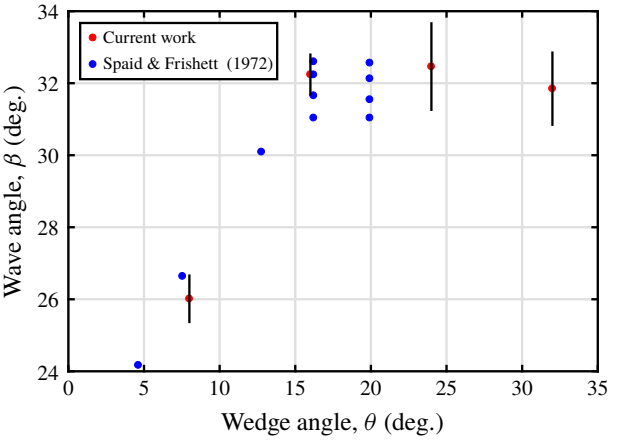


FIGURE 3. (Colour online) Initial (β) shock angles from schlieren images shown in red. Results from Spaid & Frishett (1972) shown in blue. Vertical black bars denote uncertainty.

3. Diagnostic approach: tagging velocimetry

Tagging velocimetry is a laser velocimetry technique which is typically performed in gases by tracking the fluorescence of a native, seeded or synthesized gas. Its advantage over particle-based techniques in high-speed facilities is that it is not limited by timing issues associated with tracer injection (Haertig *et al.* 2002) or reduced particle response at Knudsen and Reynolds numbers (Loth 2008) characteristic of high-speed wind tunnels. Methods of tagging velocimetry include the VENOM (Hsu *et al.* 2009*a*,*b*; Sánchez-González *et al.* 2011; Sánchez-González, Bowersox & North 2012, 2014), APART (Dam *et al.* 2001; Sijtsema *et al.* 2002; Van der Laan *et al.* 2003), RELIEF (Miles *et al.* 1987, 1989, 1993; Miles & Lempert 1997; Miles *et al.* 2000), FLEET (Michael *et al.* 2011; Edwards, Dogariu & Miles 2015), STARFLEET (Jiang *et al.* 2016), PLEET (Jiang *et al.* 2017), argon (Mills 2016), iodine (McDaniel, Hiller & Hanson 1983; Balla 2013), sodium (Barker, Bishop & Rubinsztein-Dunlop 1997), acetone (Lempert *et al.* 2002, 2003; Handa *et al.* 2014), NH (Zhang *et al.* 2017) and the hydroxyl group techniques, (Boedeker 1989; Wehrmeyer *et al.* 1999; Pitz *et al.* 2005; André *et al.* 2017) among others (Hiller *et al.* 1984; Gendrich & Koochesfahani 1996; Gendrich, Koochesfahani & Nocera 1997; Ribarov *et al.* 1999; Stier & Koochesfahani 1999; André *et al.* 2018).

For this work, krypton tagging velocimetry (KTV) was used as the velocimetry technique. The use of a metastable noble gas as a tagging velocimetry tracer was first suggested by Mills, Sukenik & Balla (2011) and Balla & Everhart (2012). KTV was first demonstrated by Parziale, Smith & Marineau (2015*a*,*b*) to measure the velocity along the centreline of an underexpanded jet of an N_2/Kr mixture. Following that work, Zahradka *et al.* (2016*a*,*b*) used KTV to make measurements of the mean and fluctuating turbulent boundary-layer profiles in a Mach 2.8 flow. Mustafa *et al.* (2017*a*) used KTV to measure seven simultaneous profiles of streamwise velocity and fluctuations in the incoming boundary layer and immediately upstream of a 24° compression corner in a $M_\infty = 2.8$, $Re_\Theta = 1750$, 99 % N_2/1 % Kr shock-wave/turbulent boundary-layer interaction. Recently, KTV was implemented in the Stevens Institute of Technology Shock Tube by Mustafa & Parziale (2017) to measure the free-stream

https://doi.org/10.1017/jfm.2018.1029 Published online by Cambridge University Press

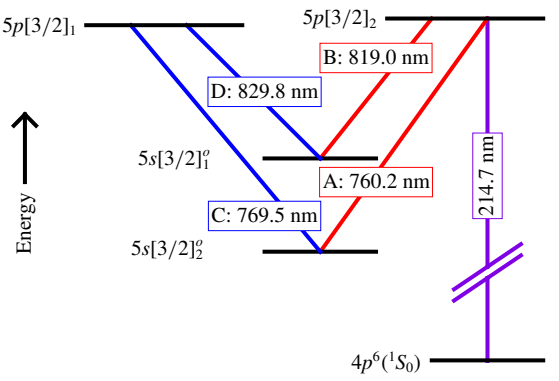


FIGURE 4. (Colour online) Energy diagram for excitation scheme. Racah nl[K]$_J$ notation, A, B, C and D represent the transitions between the states.

velocity behind a Mach 3 shock. In addition, KTV has been demonstrated to work in the free stream of the large-scale AEDC Hypervelocity Tunnel 9 at Mach 10 and Mach 14 (Mustafa *et al.* 2017*b*). Finally, preliminary two-dimensional KTV measurements in a Mach 2.8 flow over a 24° compression corner were reported in Mustafa *et al.* (2018) and simplifications to the technique are reported in Mustafa & Parziale (2018).

Following the excitation scheme used by Mustafa *et al.* (2017*a*), KTV is performed in the following steps according to the energy level diagram shown in figure 4.

(i) Seed a base flow with krypton globally, in this case 1 % Kr in 99 % N_2.

(ii) Photosynthesize metastable krypton atoms with a pulsed tuneable laser to form the tagged tracer: two-photon excitation of $4p^6(^1S_0) \rightarrow 5p[3/2]_2$ (214.7 nm) and rapid decay to resonance state $5p[3/2]_2 \rightarrow 5s[3/2]_1^o$ (819.0 nm, transition B) and metastable state $5p[3/2]_2 \rightarrow 5s[3/2]_2^o$ (760.2 nm, transition A). We estimate that the creation of the metastable atoms which comprise the 'write line' takes approximately 50 ns Chang, Horiguchi & Setser (1980). The position of the write line is marked by the fluorescence from the $5p[3/2]_2 \rightarrow 5s[3/2]_1^o$ transitions (819.0 nm, transition B), and is recorded with a camera positioned normal to the flow.

(iii) Record the displacement of the tagged metastable krypton by imaging the laser induced fluorescence (LIF) that is produced with an additional pulsed tuneable laser: excite $5p[3/2]_1$ level by $5s[3/2]_2^o \rightarrow 5p[3/2]_1$ transition with laser sheet (769.5 nm, transition C) and read spontaneous emission of $5p[3/2]_1 \rightarrow 5s[3/2]_1^o$ (829.8 nm, transition D) transitions with a camera positioned normal to the flow.

The experiments were run using two tuneable lasers to provide the 214.7 nm (write) and 769.5 nm (read) laser beams required for KTV. The write laser consisted of a frequency doubled Quanta Ray Pro-350 Nd:YAG laser and a frequency tripled Sirah PrecisionScan Dye Laser. The Nd:YAG laser pumped the dye laser with 1000 mJ pulse^{-1} at a wavelength of 532 nm. The dye in the laser was DCM with a dimethyl sulfoxide (DMSO) solvent, and the laser was tuned to output a 644.1 nm beam. Frequency tripling of the dye-laser output was performed using Sirah tripling optics (THU 205).

The write-laser beam set-up can result in approximately 10–13 mJ pulse^{-1}; however, approximately 7 mJ was used for this experiment by reducing the Nd:YAG

https://doi.org/10.1017/jfm.2018.1029 Published online by Cambridge University Press

pump-laser power. The wavelength was 214.7 nm, with a linewidth of approximately 0.045 cm^{-1}, a pulse width of approximately 7 ns and a repetition rate of 10 Hz. The write beam was focused into several narrow waists in the test section with a $f = 100$ mm fused-silica microlens array (SUSS MicroOptics Nr. 18-00127) to form the lines in the streamwise direction and a $f = 100$ mm fused-silica cylindrical lens to focus the lines in the spanwise direction. We estimate that the energy per write line was approximately 350 μJ $pulse^{-1}$.

The read laser consisted of a frequency doubled Quanta Ray Pro-350 Nd:YAG laser and a Sirah PrecisionScan Dye Laser. The Nd:YAG laser pumped the dye laser with 200 mJ $pulse^{-1}$ at a wavelength of 532 nm. The dye in the laser was Styryl 8 with a DMSO solvent, and the laser was tuned to output a 769.5 nm beam.

The read-laser beam set-up resulted in approximately 5 mJ $pulse^{-1}$, with a wavelength of 769.5 nm, a linewidth of approximately 0.025 cm^{-1}, a pulse width of approximately 7 ns and a repetition rate of 10 Hz. The read-laser beam was directed into the test section using 2 inch broadband dielectric mirrors (Thorlabs BB2-E02), and expanded to a beam of ≈40 mm diameter with a $f = -400$ mm BK7 lens. This 'read beam' re-excited the metastable Kr tracer atoms so that their displacement could be measured.

The laser and camera timing were controlled by a pulse-delay generator (SRS DG645). The intensified camera used for all experiments was a 16-bit Princeton Instruments PIMAX-4 1024 × 1024 with an 18 mm grade 1, Gen III extended red filmless intensifier w/P46 phosphor (PM4-1024i-HR-FG-18-P46-CM). The lens used is a Nikon NIKKOR 24–85 mm f/2.8-4D in 'macro' mode and positioned approximately 200 mm from the write/read location which was at the centre of the test section at Port 2 in figure 1. Two high-precision 800 nm longpass filters (Thorlabs FELH0800, transmission of 3.5e-4 % at the read-laser wavelength of 769.5 nm) were placed in series between the lens and the intensifier to minimize the noise resulting from the read-laser pulse reflection and scatter from solid surfaces. The gain was set to 100 % with 1 × 6 (streamwise × wall-normal) pixel binning and only recording the read images to ensure a 10 Hz frame rate. A set of write images were recorded with the tunnel on prior to each set of experiments. The camera gate was opened for 20 ns immediately following the read-laser pulse to capture the spontaneous emission of $5p[3/2]_1 \rightarrow 5s[3/2]_1^o$ (829.8 nm) transitions.

4. Boundary-layer results

In this section, we present a baseline boundary-layer profile of streamwise velocity and fluctuations. For the boundary-layer results, the write/read delay was set to 500 ns. The KTV set-up formed ten lines with appropriate signal to noise ratio (SNR). A sample read exposure is presented in figure 5(*a*). To process the KTV exposures, the line centres were found in the following way:

(i) Crop the image to an appropriate field of view.
(ii) Apply a two-dimensional Wiener adaptive-noise removal filter.
(iii) Convert the images to double precision numbers and normalize the intensity to fall in the range of 0–1.
(iv) Apply the Gaussian peak finding algorithm from O'Haver (1997) to find the line centres for the top row using the read lines in the top row of each image as a first guess.
(v) Proceeding from the top down, apply the Gaussian peak finding algorithm from O'Haver (1997) to find the line centres for each row using the line centre location immediately above as the guess.

https://doi.org/10.1017/jfm.2018.1029 Published online by Cambridge University Press

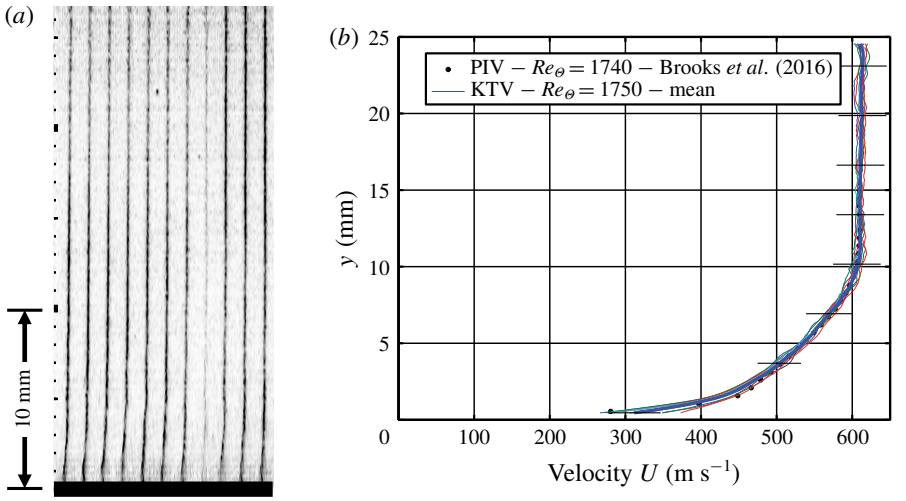


FIGURE 5. (Colour online) (*a*) Example of KTV boundary-layer fluorescence exposure. Major tick marks are 10 mm. Flow is left to right. Inverted intensity scale. Wall marked as black. (*b*) Dimensional velocity of the Mach 2.8 turbulent boundary layer. Error bars in black.

The dimensional velocity is presented in figure 5(*b*) as measured by KTV from the present work and PIV from Brooks *et al.* (2014, 2015, 2016, 2018) in the same facility. Figure 5(*b*) shows that the boundary-layer thickness in the incoming flow, δ, is ≈ 10.25 mm. This is the value that is used to normalize the distance coordinates in subsequent figures and analyses. Error bars for the KTV measurements are calculated in the same fashion as Zahradka *et al.* (2016*a*) as

$$\widetilde{U}_{KTV} = \left[\left(\widetilde{\Delta x} \frac{\partial U}{\partial \Delta x} \right)^2 + \left(\widetilde{\Delta t} \frac{\partial U}{\partial \Delta t} \right)^2 + \left(v'_{rms} \frac{\partial U}{\partial y} \Delta t \right)^2 \right]^{1/2}, \tag{4.1}$$

where uncertainty estimates of a variable are indicated with a tilde.

The uncertainty in the measured displacement distance, $\widetilde{\Delta x}$, of the metastable tracer is estimated as the 95 % confidence bound on the write and read locations from the Gaussian fits. The uncertainty in time, $\widetilde{\Delta t}$, is estimated to be the camera gate width, 20 ns, causing fluorescence blurring as considered in Bathel *et al.* (2011). The third term in (4.1) is the uncertainty in the streamwise velocity due to wall-normal fluctuations in the *xy*-plane. This formulation is taken from Hill & Klewicki (1996) and Bathel *et al.* (2011). The wall-normal fluctuations used in (4.1) (v'_{rms}) are conservatively estimated to be 5 % of the edge velocity, which is supported by DNS (Martin 2007) and PIV experiments (Brooks *et al.* 2016).

The error in the KTV measurement is approximately 5 % in the free stream, the boundary-layer wake region and the boundary-layer logarithmic region. The error in KTV measurement increases to approximately 10 % nearest to the wall. The increase nearest to the wall is mostly due to the third term in (4.1). There is an appreciable increase in the wall-normal fluctuations and increase in velocity gradient.

The velocity data for the boundary layer can be compared to the law of the wall in the logarithmic region, $U^+ = (1/\kappa)\ln(y^+) + C$, by using the van Driest I transformation, with $y^+ = \rho_w u_\tau y/\mu_w$ and $U^+ = U/u_\tau$. Following Bradshaw (1977) and

https://doi.org/10.1017/jfm.2018.1029 Published online by Cambridge University Press

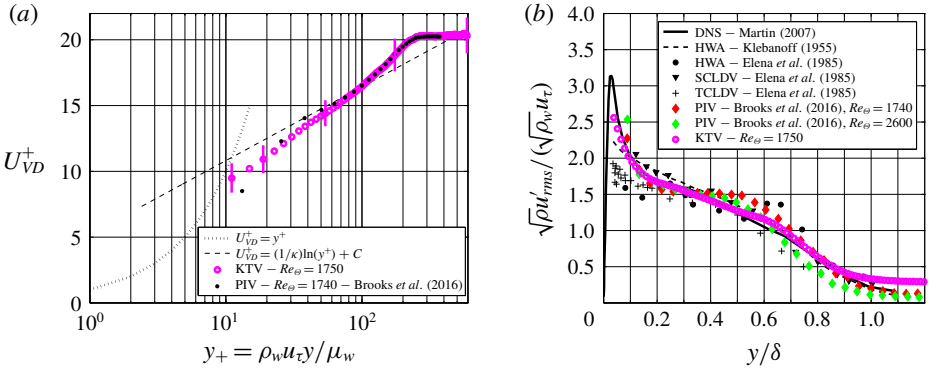


FIGURE 6. (Colour online) (*a*) The van Driest scaling of the mean velocity. (*b*) Morkovin scaling of streamwise fluctuations.

Huang & Coleman (1994), the van Driest I transformed velocity is written as

$$U^+_{VD} = \frac{1}{R}\left[\sin^{-1}\left(\frac{R(U^+ + H)}{\sqrt{1 + R^2H^2}}\right) - \sin^{-1}\left(\frac{RH}{\sqrt{1 + R^2H^2}}\right)\right], \tag{4.2}$$

where $R = M_\tau\sqrt{(\gamma - 1)Pr_t/2}$, $H = B_q/((\gamma - 1)M^2_\tau)$, $M_\tau = u_\tau/c_w$ and $B_q = q_w/(\rho_w c_p u_\tau T_w)$. We assume the turbulent Prandtl number is $Pr_t = 0.87$, and, assuming the Reynolds analogy holds, the heat-flux number is $B_q = c_f\rho_e U_e(T_w - T_r)/(2Pr_e\rho_w u_\tau T_w)$ (Schlichting 2000). Here, c_w is the sound speed at the wall, c_p is the constant pressure specific heat, T_w is the wall temperature, T_e is the edge temperature, T_r is the recovery temperature, c_f is the skin friction coefficient, U_e is the edge velocity, Pr_e is the edge Prandlt number, ρ_w is the density at the wall, ρ_e is the edge density, q_w is the heat transfer rate at the wall and y is the ratio of specific heats. The friction velocity, u_τ, is calculated in the same way as Zahradka *et al.* (2016*a*) using the von Kármán (1934)–Schoenherr (1932) equation under the van Driest II transformation (table 1). Based on these values, the viscous length scale is $\eta \approx \nu_w/u_\tau \approx 40$ μm. For comparison, the wall-normal spatial resolution of this KTV implementation is ≈170 μm due to camera resolution. The streamwise spatial resolution for a single KTV line is estimated to be ≈10 μm, which is the uncertainty in line-centre location. These resolutions approach the viscous length scale in the flow. We should note that the streamwise spatial resolution for tracking turbulent structures as a field (as is the case in the longitudinal correlations and forthcoming POD analysis) is 1.2 mm due to measurement spacing (figure 5).

The transformed KTV- and PIV-derived velocity profiles are presented in figure 6(*a*). Also, in figure 6(*a*), we plot the viscous sublayer as $U^+_{VD} = y^+$ as well as applying (4.2) to the logarithmic law as

$$U^+_{VD} = \frac{1}{\kappa}\ln(y^+) + C, \tag{4.3}$$

with $\kappa = 0.41$ and $C = 5.2$. The transformed velocity follows the law of the wall in the logarithmic region with good agreement.

In figure 6(*b*), we present the streamwise-velocity-fluctuation results that are non-dimensionalized by the Morkovin (Morkovin 1962) scaling and compare those to the literature (Klebanoff 1955; Elena, Lacharme & Gaviglio 1985; Martin 2007; Brooks *et al.* 2016). In this work, we were able to resolve far closer to the wall than in the previous KTV effort by Zahradka *et al.* (2016*a*). The agreement between the fluctuation data from the literature and KTV is good to down to $y/\delta \approx 0.05$.

https://doi.org/10.1017/jfm.2018.1029 Published online by Cambridge University Press

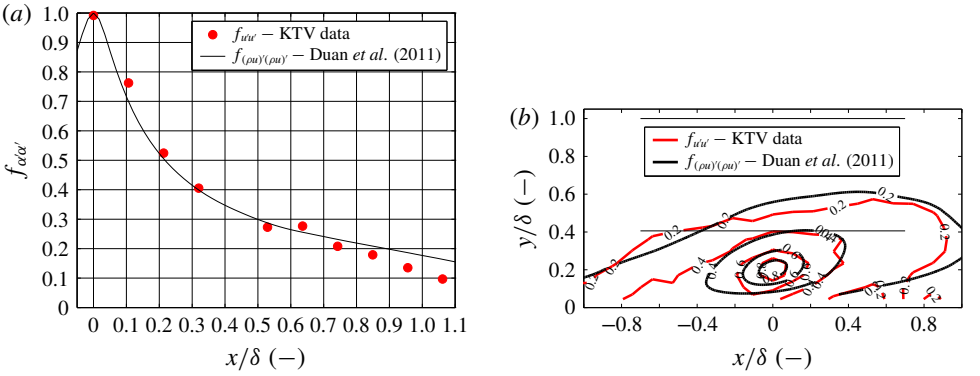


FIGURE 7. (Colour online) (*a*) Longitudinal correlation for $y/\delta \approx 0.2$. As a means of first comparison, $f_{u'u'}$ from the present KTV boundary-layer data is compared to $f_{(\rho u)'(\rho u)'}$ from Duan, Beekman & Martin (2011). (*b*) Contours of correlation. Thin horizontal lines mark the boundary-layer edge and approximate wake-region boundary. KTV data in red, DNS data in black.

With the ability to write multiple lines, the longitudinal correlation coefficient can be calculated as

$$f(\boldsymbol{x}, r) = \frac{\overline{u'(\boldsymbol{x})u'(\boldsymbol{x}+r)}}{\overline{u'^2}} = \frac{R_{u'u'}}{\overline{u'^2}} \tag{4.4}$$

by using the spacing between each write line, r. The longitudinal correlation of the streamwise-velocity data is presented in figure 7(*a*) for $y/\delta \approx 0.2$. As a means of first comparison, $f_{u'u'}$ from the present KTV boundary-layer data is compared to $f_{(\rho u)'(\rho u)'}$ from Duan *et al.* (2011). It should be noted that the work from Duan *et al.* (2011) is at different conditions, $M_\infty = 2.97$, $Re_\Theta = 3030$.

Moreover, because the flow field should have forward and backward symmetry, the number of points used for the longitudinal correlation can be increased from 10 to 19 by performing the correlation in (4.4) from left-to-right and also right-to-left and concatenating the datasets. This correlation is performed for the field recorded in figure 5 for $y/\delta \approx 0.2$ and presented in figure 7(*b*). Thin horizontal lines in figure 7(*b*) mark the boundary-layer edge at $y/\delta = 1$ and also the approximate location of the wake-region boundary at $y/\delta \approx 0.41$. Contours of $f_{(\rho u)'(\rho u)'}$ as computed by DNS data from Duan *et al.* (2011) are plotted in black, and contours of $f_{u'u'}$ as measured from KTV data are plotted in red. The KTV data have more scatter, as expected, but the orientation of the contours is quite similar, indicating that the average angle of turbulent structures is also similar.

In this section, KTV data were compared to those in the literature for a supersonic turbulent boundary layer. From this, we conclude that the nature of the incoming flow can be considered a nominal supersonic turbulent boundary layer enabling the study of shock-wave/turbulent boundary-layer interaction.

5. Shock-wave/turbulent boundary-layer interaction results

In this section, we present the results from experiments designed to investigate turbulent, supersonic corner flows at four different angles: 8°, 16°, 24° and 32°. This is done by fixing a wedge of the appropriate geometry in Port 2 of the M3CT

https://doi.org/10.1017/jfm.2018.1029 Published online by Cambridge University Press

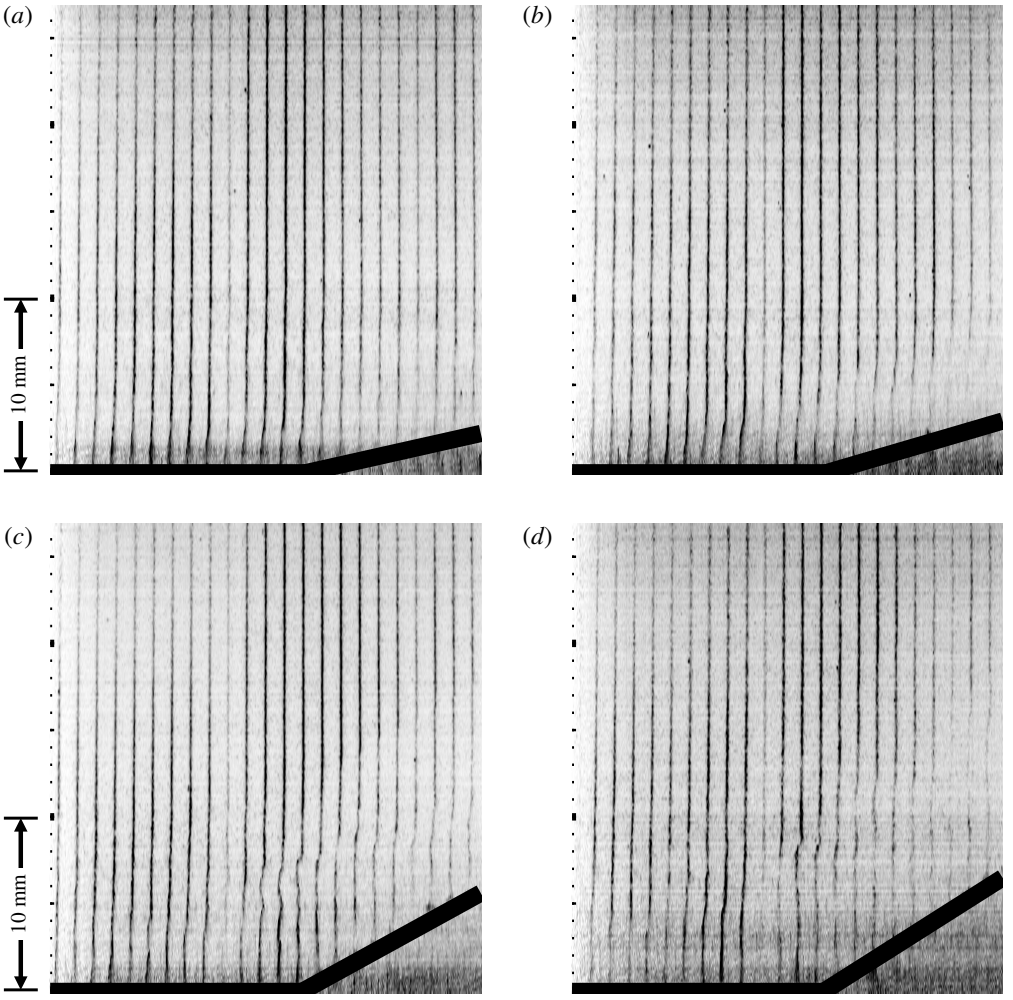


FIGURE 8. Sample instantaneous shock-wave/turbulent boundary-layer interaction fluorescence exposures for the (*a*) 8°, (*b*) 16°, (*c*) 24° and (*d*) 32° corners, respectively. These are ostensibly boundary-layer profiles traces with a 500 ns prescribed delay between the write and read steps. Major tick marks are 10 mm. Flow is left to right. Inverted intensity scale. Wall marked as black. Animations of instantaneous fluorescence exposures and corresponding velocity profiles are provided in the supplementary material (movie 1, movie 2, movie 3 and movie 4 for the 8, 16, 24 and 32 degree corners, respectively).

(see figure 1). The root of the corner flow ($x/\delta = 0$) is placed near the centre of the boundary-layer measurement location presented in § 4.

Figure 8 shows sample KTV read exposures for each case. This is the visualization of the $5p[3/2]_1 \rightarrow 5s[3/2]_1^o$ (829.8 nm) transition. Mach 2.8 flow is left to right and the walls in each corner flow are marked in black. These data are reduced by following the same procedure as in § 4 for tracing the profiles in the write and read images. Animations of instantaneous fluorescence exposures and corresponding velocity profiles are provided as in the supplementary material (movie 1, movie 2, movie 3 and movie 4 for the 8, 16, 24 and 32 degree corners, respectively), available online at https://doi.org/10.1017/jfm.2018.1029.

https://doi.org/10.1017/jfm.2018.1029 Published online by Cambridge University Press

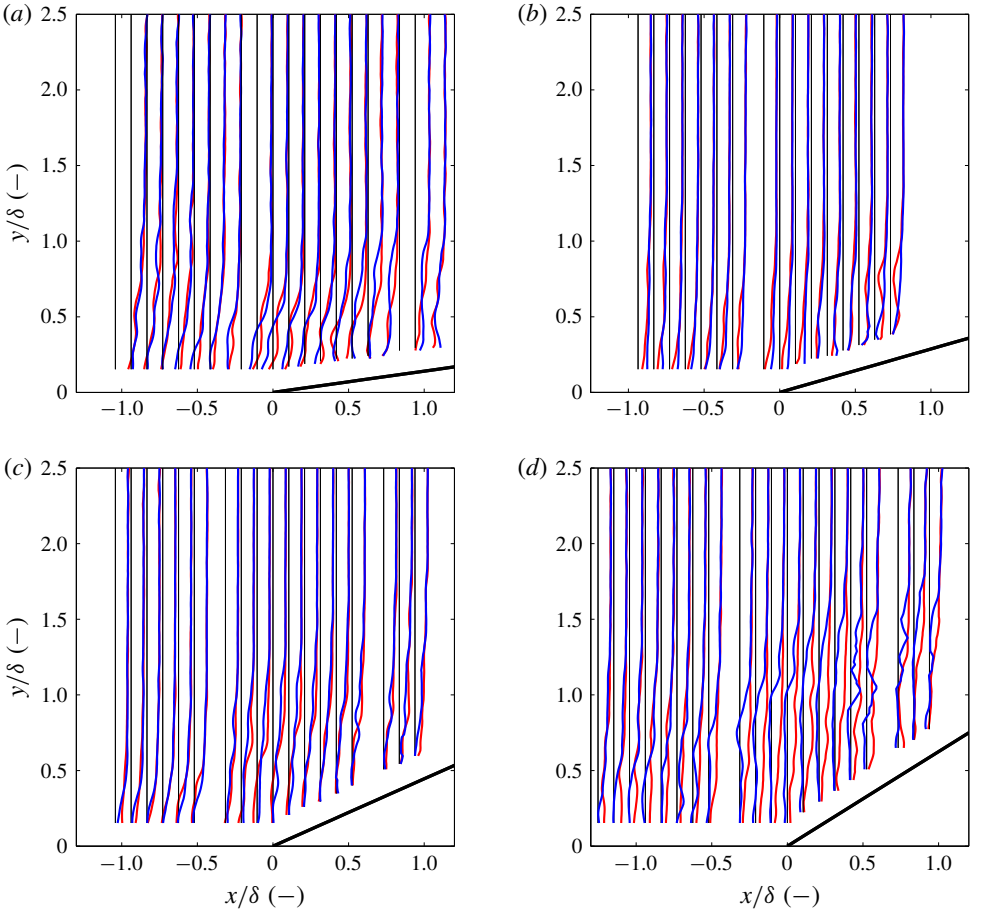


FIGURE 9. (Colour online) Sample non-dimensional $(u/(12U_\infty))$, instantaneous shock-wave/turbulent boundary-layer interaction velocity profiles represented in blue and red for the (*a*) 8°, (*b*) 16°, (*c*) 24° and (*d*) 32° corners, respectively. Thin vertical black line represents the write location. Flow is left to right.

Examples of non-dimensional instantaneous velocity profiles $(u/(12U_\infty))$ are presented in figure 9. For each corner angle, we show the write location marked as a thin, vertical black line and two randomly selected, example instantaneous velocity profiles in blue and red. This is intended to visualize relative unsteadiness of each corner flow. Results are not presented within $y/\delta < 0.1$ because the signal to noise ratio was too low to provide data with high confidence. In addition, there is a missing velocity profile every 10 mm because there is a gap between the microlens arrays that yields insufficient focusing and thus low SNR.

In figure 10, we present non-dimensional mean-velocity profiles $(u/(12U_\infty))$. For each corner angle, we show the write location marked as a thin, vertical black line and the mean-velocity profile as a thicker blue line. In the 8° and 16° cases, there are no clearly apparent points of inflection in the mean profiles. In the 24° case, near to the root $(-0.5 \lesssim x/\delta \lesssim 0.5)$, and to a much greater extent in the 32° case (the field of view), there appear to be clear points of inflection in the mean boundary-layer profiles.

https://doi.org/10.1017/jfm.2018.1029 Published online by Cambridge University Press

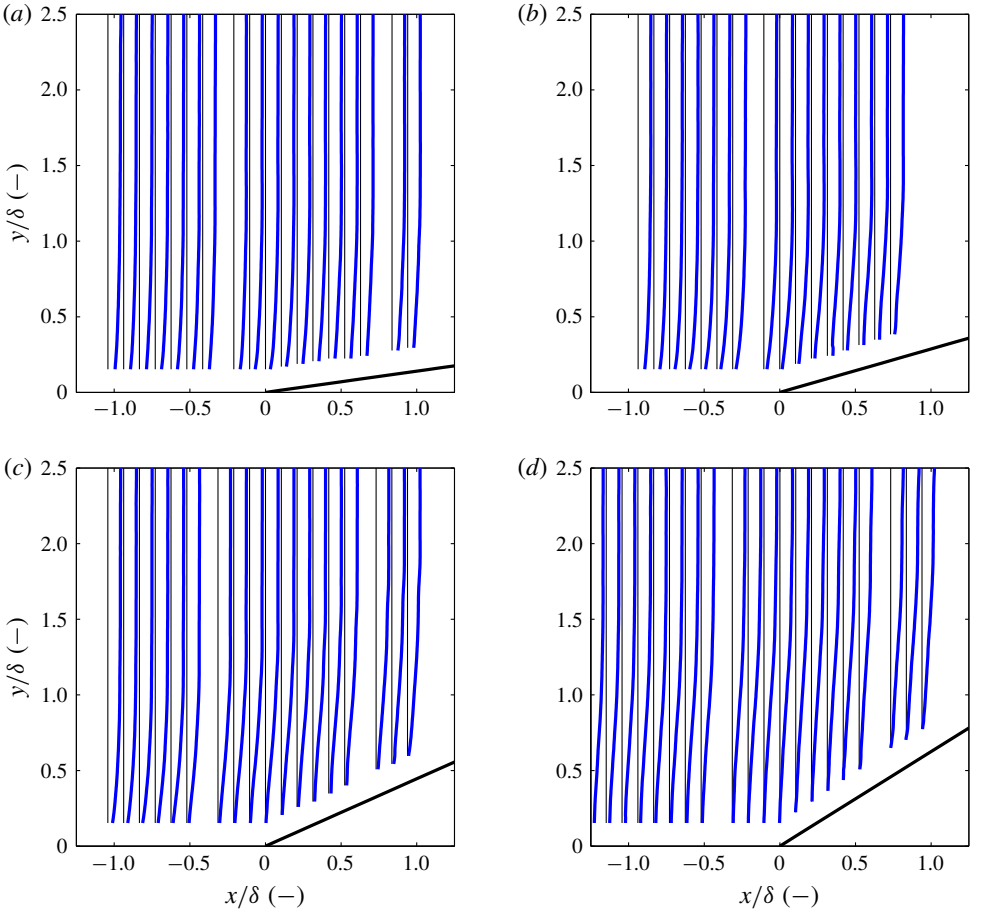


FIGURE 10. (Colour online) Non-dimensional $(u/(12U_\infty))$, mean shock-wave/turbulent boundary-layer interaction velocity profiles for the (*a*) 8°, (*b*) 16°, (*c*) 24° and (*d*) 32° corners, respectively. Thin vertical black line represents the write location. Flow is left to right. Error bars are not plotted because they are not visible at the present scale. We estimate the uncertainty as 5 % in the free stream and 15 % near the wall.

In figure 11(*a*) we show the distribution of the instantaneous normalized velocity at the root (u_c/U_∞) for all corner angles. We define a parameter to quantify the flow separation as $t_s = C_s/C_T$, where C_s is the number of counts (or snapshots) in which $u_c < 0$ and C_T is the total number of counts. This represents the percentage of the total snapshots in which the flow near the root is separated. It is observed that for the 8° case, the flow for all practical purposes is not separated. Beginning with the 16° case, the mean of the velocity shifts to the left as separation becomes more prominent. We also show the scaling of t_s with wedge angle in figure 11(*b*).

Contours of the streamwise component of turbulent kinetic energy (sTKE), $(u'_{rms})^2/(2U_\infty^2)$, are presented in figure 12. For each case, very close to the wall on the ramp, there is a notable increase in fluctuations. This is most likely an artefact of the residual noise from the KTV read step. Despite this, in the 16°, 24° and 32° cases, a shear layer can clearly be identified as a maximum in fluctuations along a ray inclined at an angle similar to that of the corner angle. No such shear layer

https://doi.org/10.1017/jfm.2018.1029 Published online by Cambridge University Press

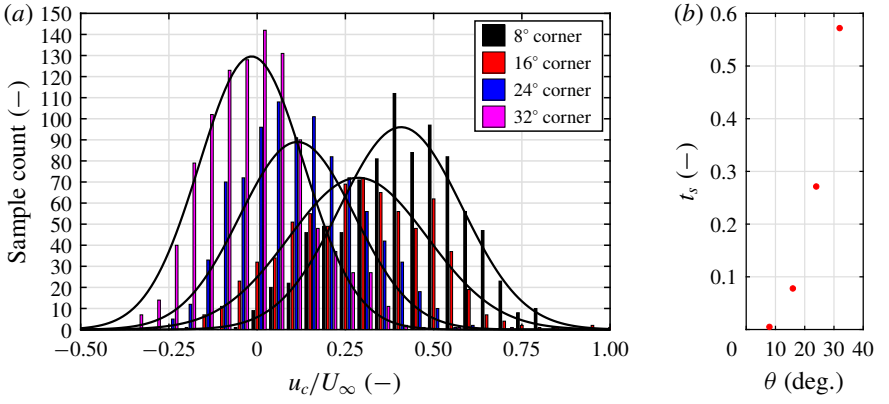


FIGURE 11. (Colour online) (*a*) Distribution of normalized velocity (u_c/U_∞) near the root for all wedge angles. (*b*) Scaling of t_s with corner angle θ.

Wedge angle (Degrees)	x_{01} (−)	θ_s (Degrees)
16	−0.97 (± 0.30)	18.2 (± 3.9)
24	−1.24 (± 0.14)	21.8 (± 1.9)
32	−1.71 (± 0.27)	26.2 (± 3.6)

TABLE 2. Shear-layer origin, x_{01}, and angle θ_s. Uncertainties estimated as the 95 % confidence intervals in the linear fits.

was observed in the 8° case. Also superimposed on the contour plots is a white demarcation line denoting the points where $u'_{rms} = 0.02U_\infty$, i.e. when the turbulence intensity reaches the level of the noise in the tunnel.

To characterize the shear layers, two parameters were determined: θ_s, which is the angle of the shear-layer coordinate system (x', y') relative to the laboratory coordinate system (x, y), and x_{01}, which is the origin of the (x', y') coordinate system. The parameters were found by fitting an equation of the form $y = \tan\theta_s(x - x_{01})$ to the spatial locations of the maximum sTKE at each streamwise location. The results for the corners are overlaid on the sTKE contours in figure 12 and the values for θ_s and x_{01} are given in table 2. In performing this analysis it is assumed that the sTKE ($u'^2/(2U_\infty^2)$) is an acceptable surrogate for the total TKE ($(u'^2 + v'^2 + w'^2)/(2U_\infty^2)$).

In Helm, Martin & Dupont (2014), the researchers show that the shear layer over a 24° corner may be collapsed in a self-similar fashion. They apply a coordinate transformation to the two-dimensional velocity calculations in the laboratory frame to determine the velocity in the shear-layer coordinate system. Unfortunately, in this work a rotation may not be applied as the KTV measurements were one-dimensional. Despite this, we use the velocity in the laboratory frame as a surrogate for the velocity in the shear-layer coordinate system and attempt to identify self-similarity to first approximation. In figure 13, we attempt to collapse the U/U_2 and u'^2_{rms}/U_2^2 profiles to a single curve, where U is the mean velocity and U_2 is the velocity downstream of the shock as calculated by the inviscid flow relations for the measured shock angle. The similarity variable used is $\zeta = y'/(x' - x'_{02})$, where x_{02} is the imaginary origin of

https://doi.org/10.1017/jfm.2018.1029 Published online by Cambridge University Press

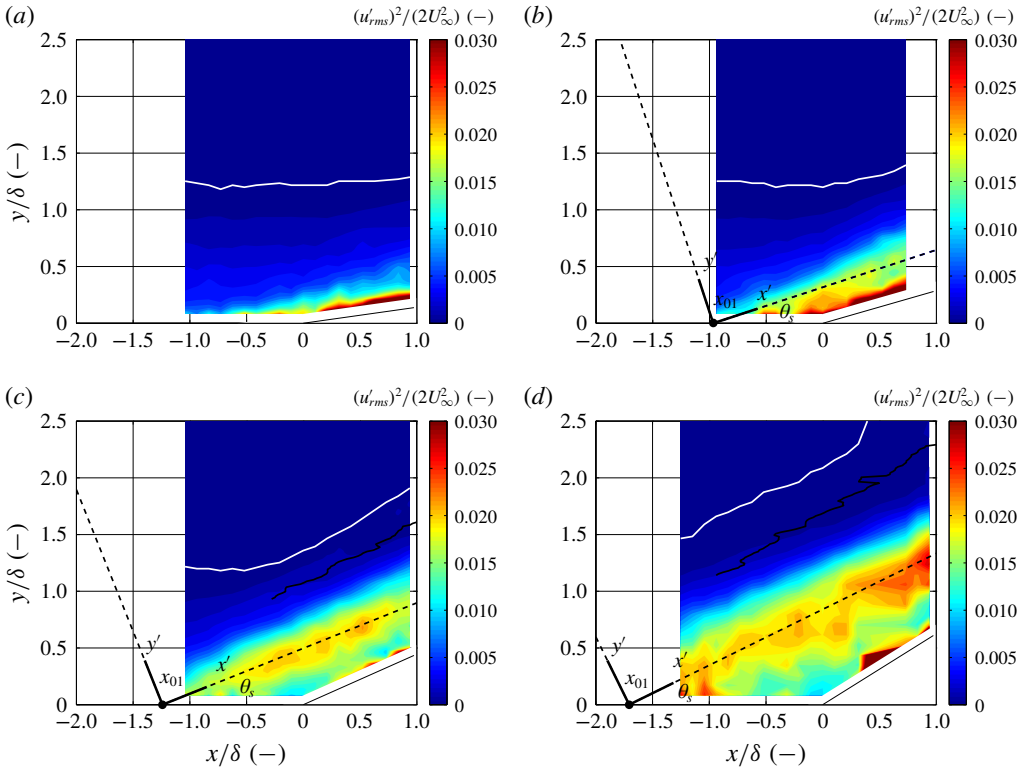


FIGURE 12. (Colour online) Contours of the non-dimensional streamwise turbulent kinetic energy (sTKE) $(u'_{rms})^2/(2U_\infty^2)$) for the (*a*) 8°, (*b*) 16°, (*c*) 24° and (*d*) 32° corners, respectively. The shear-layer coordinate system fitted to the maximum sTKE is overlaid. Flow is left to right. Mean shock position shown in black. White line marks y_u/δ which is the wall-normal location above which the streamwise-velocity fluctuations are less than 2 % of the free-stream velocity, or $u'_{rms} = 0.02U_\infty$.

the shear layer, which is computed by iterating until the profiles collapse. It should be noted that unlike in Helm *et al.* (2014), u'_{rms} is the x component of the fluctuating velocity in the (x, y) coordinate system, not the x' component of the fluctuating velocity in the (x', y') coordinate system. Compared to Helm *et al.* (2014), figure 13 shows more scatter and the collapse is not qualitatively as good. Despite this and the limitations in the analysis, self-similar behaviour is apparent to a first approximation.

6. Wall-normal integrated streamwise turbulent kinetic energy

In this section, we present an analysis of the sTKE $(u'^2_{rms}/2)$ in profile form (as opposed to the contours presented earlier) to identify trends in sTKE with compression-corner angle. We define a figure of merit as the wall-normal integrated sTKE at a particular streamwise location as

$$\overline{\mathrm{sTKE}} = \int_{y_l/\delta}^{y_u/\delta} \frac{u'^2_{rms}}{2U_\infty^2}\, \mathrm{d}\left(\frac{y}{\delta}\right), \tag{6.1}$$

where the lower limit, y_l/δ, is the lowest wall-normal location where KTV data were collected, and the upper integration limit, y_u/δ, is the wall-normal location

https://doi.org/10.1017/jfm.2018.1029 Published online by Cambridge University Press

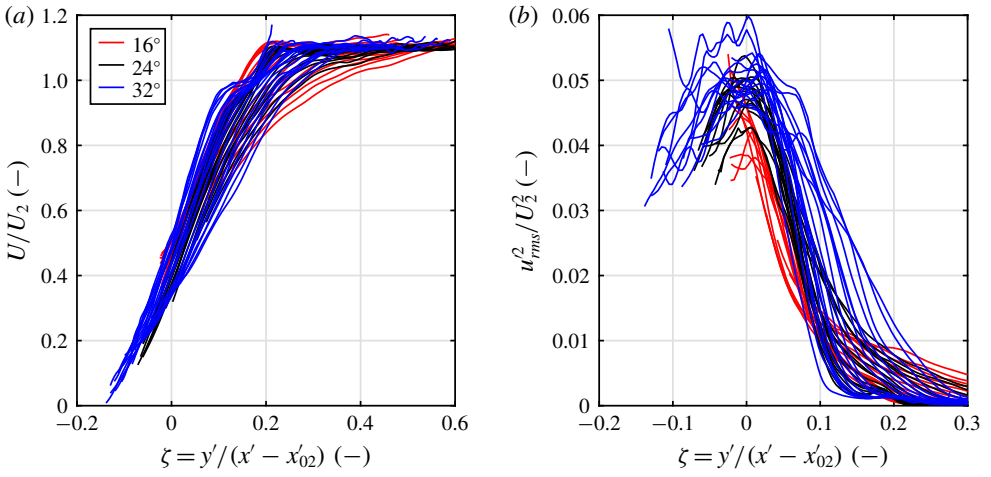


FIGURE 13. (Colour online) (*a*) The U/U_2 profiles plotted against the similarity variable ζ for the 16°, 24° and 32° corners. (*b*) The u'^2_{rms}/U_2^2 profiles plotted against the similarity variable ζ for the 16°, 24° and 32° corners. Here, U_2 is the downstream velocity as calculated from oblique shock relations for a Mach 2.8 flow and the shock angle as measured form the schlieren images.

x/δ (−)	Fit
0	$\overline{\text{sTKE}}/\overline{\text{sTKE}}_{BL} = 0.99\exp(7.91 \times 10^{-2}\theta)$
0.5	$\overline{\text{sTKE}}/\overline{\text{sTKE}}_{BL} = 0.77\exp(9.35 \times 10^{-2}\theta)$

TABLE 3. Sclaing relations for $\overline{\text{sTKE}}$.

above which the streamwise velocity fluctuations are less than 2 % of the free-stream velocity, or $u'_{rms} = 0.02U_\infty$. A threshold of 2 % was chosen because it is just above the measured free-stream streamwise-velocity-fluctuation level in this wind tunnel, which is 1.0–1.5 %. The threshold, y_u/δ, is presented as a white line in the TKE contours in figure 12. As such, we isolate the streamwise fluctuations in the boundary layer and the shock-wave/boundary-layer interaction from those in the wind tunnel free stream and the measurement noise. We note that the $\overline{\text{sTKE}}$ results presented herein are relatively insensitive to the choice of this threshold in the range of 1.5–4.0 %.

Ultimately, this figure of merit is designed to identify turbulence amplification by accounting for both the amplitude of the velocity fluctuations and shear-layer width for the different geometries. In figure 14(*a*) we present the $\overline{\text{sTKE}}$ for each streamwise location. It is observed that $\overline{\text{sTKE}}$ increases with increasing x/δ. In figure 14(*b*), $\overline{\text{sTKE}}$ is plotted against the corner angle at locations downstream of and at the corner. We normalize by the $\overline{\text{sTKE}}$ in the boundary layer (figure 6*b*) to find the effect of compression-corner angle on wall-normal integrated streamwise turbulence amplification. The trend of $\overline{\text{sTKE}}$ with compression-corner angle is found to be an exponential. The parameters for this scaling are given in table 3 for the two locations. Sensibly, the coefficients of the exponentials in table 3 are close to unity (within experimental error) which implies no amplification at zero compression-corner angle.

https://doi.org/10.1017/jfm.2018.1029 Published online by Cambridge University Press

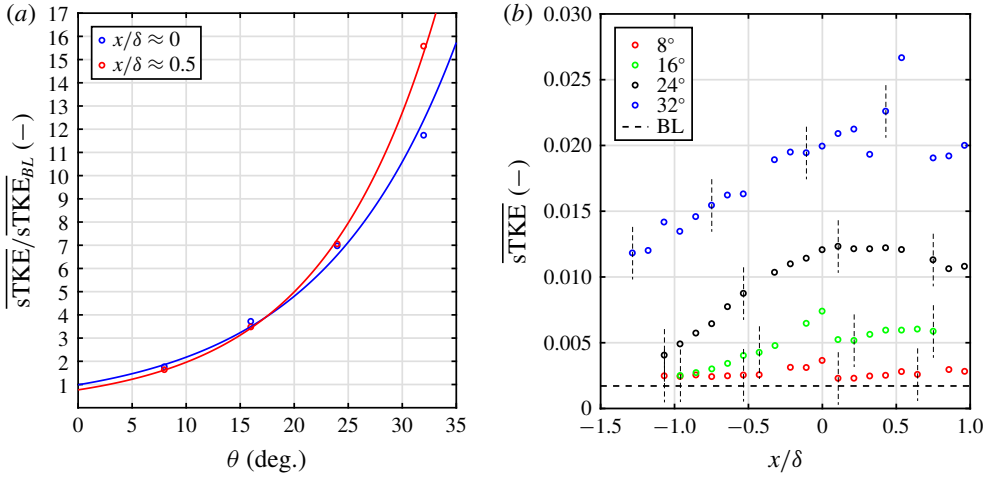


FIGURE 14. (Colour online) (*a*) Variation of $\overline{\text{sTKE}}$ along the streamwise direction for 8°, 16°, 24° and 32° corners. Error bars shown as vertical dashed lines. (*b*) Scaling of $\overline{\text{sTKE}}$ with wedge angle for locations at and downstream of the root, where the values at $x/\delta \approx 0$ are the averages of the points adjacent to and at the root.

7. Proper orthogonal decomposition

The proper orthogonal decomposition (POD) technique can be used to extract spatial and temporal structures from a turbulent flow field (Lumley 1967; Berkooz *et al.* 1993; Taira *et al.* 2017). This approach decomposes the original vector or scalar field into a weighted, linear sum of basis functions, or modes. In the present work, the instantaneous streamwise-velocity fields are recorded at 10 Hz so they are nominally uncorrelated in time; thus, the snapshot method of Sirovich (1987) was chosen to analyse the data.

Following the terminology in Sirovich (1987) and Stöhr, Sadanandan & Meier (2011), the streamwise-velocity fields are decomposed into a mean and fluctuating component as

$$u_i(x, y) = \overline{u}(x, y) + u_i'(x, y). \tag{7.1}$$

In the datasets presented here, there are p points in the streamwise direction and q points in the wall-normal direction ($M = p \times q$ total grid points) with N number of snapshots ($i = 1 \ldots N$). The fluctuating streamwise-velocity field, $u_i'(x, y)$, is reshaped into a matrix, $\boldsymbol{U}'$, with elements $U_i'(X_n)$ where the $n = 1 \ldots M$ points for each snapshot form a row for $i = 1 \ldots N$ rows, so $\boldsymbol{U}'$ is of dimensions $N \times M$ and can be written as

$$\boldsymbol{U}' = \begin{bmatrix} u_1'(x_1, y_1) & u_1'(x_2, y_1) & .. & u_1'(x_p, y_q) \\ u_2'(x_1, y_1) & u_2'(x_2, y_1) & .. & u_2'(x_p, y_q) \\ \vdots & \vdots & .. & \vdots \\ \vdots & \vdots & .. & \vdots \\ u_N'(x_1, y_1) & u_N'(x_2, y_1) & .. & u_N'(x_p, y_q) \end{bmatrix} = \begin{bmatrix} U_1'(X_1) & U_1'(X_2) & ... & U_1'(X_M) \\ U_2'(X_1) & U_2'(X_2) & ... & U_2'(X_M) \\ \vdots & \vdots & ... & \vdots \\ \vdots & \vdots & ... & \vdots \\ U_N'(X_1) & U_N'(X_2) & ... & U_N'(X_M) \end{bmatrix}. \tag{7.2}$$

https://doi.org/10.1017/jfm.2018.1029 Published online by Cambridge University Press

Where $U_1'(X_2)$ is the value of u' at the spatial location X_2 in the 1st snapshot and so on. We assume that the velocity may be written as

$$U_i'(X_n) = \sum_{j=1}^{N} a_{ij}\phi_j(X_n). \tag{7.3}$$

Here, $\phi_j(X_n)$ is the jth eigenfunction (or mode) and a_{ij} is the coefficient of the jth mode that corresponds to the ith snapshot of the velocity field. The goal is to prescribe a condition that would allow us to identify flow structures within a mode ϕ_j. The condition that achieves this, following Berkooz *et al.* (1993), is that the decomposition be optimal. Optimal here means that for a given number of modes, the decomposition will contain the most kinetic energy possible out of all possible decompositions. When this condition is met, the decomposition in (7.3) will represent the proper orthogonal decomposition. To impose the optimality condition, the Fredholm integral eigenvalue problem must be solved,

$$\int_{\Omega} R(X_m, X_n)\phi_j(X_n)\,\mathrm{d}\Omega = \overline{\lambda}\phi_j(X_m). \tag{7.4}$$

Here, m is a free index ($m = 1 \ldots M$), $\overline{\lambda}$ is the eigenvalue of mode j and Ω is the region of integration, which is the flow field space. $R(X_m, X_n)$ is the two-point correlation defined as,

$$R(X_m, X_n) = \overline{U'(X_m)U'(X_n)}. \tag{7.5}$$

To solve the eigenvalue problem, the integral in (7.4) must be approximated by a finite sum. This is accomplished by writing

$$\sum_{n=1}^{M} R(X_m, X_n)\phi_j(X_n)\Delta\Omega_n = \overline{\lambda}\phi_j(X_m). \tag{7.6}$$

Here, we have divided the domain into M subdivisions, each of size $\Delta\Omega_n$. Each subdivision encompasses a spatial (measurement) location X_n. To solve the eigenvalue problem in MATLAB, the matrix $\boldsymbol{R}$, whose elements are $R(X_m, X_n)$, can be constructed from $\boldsymbol{U}'$ as,

$$\boldsymbol{R} = \frac{1}{N}\boldsymbol{U}'^{T}\boldsymbol{U}' \tag{7.7}$$

where the superscript T denotes the matrix transpose. The dimensions of $\boldsymbol{R}$ are $M \times M$. Using this, the eigenvalue problem of (7.6) can be written as,

$$\boldsymbol{R}\overline{\boldsymbol{W}}\boldsymbol{\phi_j} = \overline{\lambda}\boldsymbol{\phi_j}. \tag{7.8}$$

Here $\overline{\boldsymbol{W}}$ is a diagonal matrix of dimensions $M \times M$ which contains the $\Delta\Omega_n$ values for all the spatial locations and $\boldsymbol{\phi_j}$ is a $M \times 1$ column vector whose elements are $\phi_j(X_n)$ $(n = 1 \ldots M)$. From $\overline{\boldsymbol{W}}$ can extract a constant $\Delta\Omega$ and can write the eigenvalue problem as,

$$\Delta\Omega\boldsymbol{R}\boldsymbol{W}\boldsymbol{\phi_j} = \overline{\lambda}\boldsymbol{\phi_j}. \tag{7.9}$$

Now $\boldsymbol{W}$ contains the spatial weights of each location relative to the constant $\Delta\Omega$ and has no units. Furthermore, we can combine $\Delta\Omega$ with the eigenvalue ($\lambda = \overline{\lambda}/\Delta\Omega$) to write,

$$\boldsymbol{R}\boldsymbol{W}\boldsymbol{\phi_j} = \lambda\boldsymbol{\phi_j}. \tag{7.10}$$

https://doi.org/10.1017/jfm.2018.1029 Published online by Cambridge University Press

Note that the eigenvalue λ has units of $\mathrm{m}^2\ \mathrm{s}^{-2}$ in this work. Equation (7.10) represents the general eigenvalue problem and can be solved once $\boldsymbol{W}$ is determined. In the case of this work, the laser lines are evenly spaced except at two locations in the flow field. These locations correspond to the missing velocity profiles because of the gap in the microlens array. Therefore the spatial points in the two laser lines adjacent to the missing line have to be weighted by a factor of 1.5 more than all the other points in order to integrate over the entire domain. However it was found that, by neglecting or adding the different spatial weights of the aforementioned points, the changes in the results were negligible, therefore in this work $\boldsymbol{W}$ was the identity matrix and the eigenvalue problem further simplifies to,

$$\boldsymbol{R}\boldsymbol{\phi}_j = \lambda \boldsymbol{\phi}_j. \tag{7.11}$$

The dimensions of $\boldsymbol{R}$ are $M \times M$, which in this work are $\approx 2500 \times 2500$. This a fairly large matrix whose eigenvalue computation is expensive. To address this computational cost, Sirovich (1987) suggested solving the following nominally equivalent eigenvalue problem,

$$\boldsymbol{C}\boldsymbol{e}_j = \lambda \boldsymbol{e}_j. \tag{7.12}$$

Where $\boldsymbol{C} = (1/N)\boldsymbol{U}'\boldsymbol{U}'^T$, with dimensions of $N \times N$ and $\boldsymbol{e}_j$ is the eigenfunction (represented here as a column vector). In this work $N \approx 900$ and therefore (7.12) is less computationally expensive than (7.11). The POD modes can be derived from (7.12) as (Stöhr *et al.* 2011),

$$\phi_j(X_n) = \frac{1}{\lambda_j N} \sum_{i=1}^{N} a_{ij} U_i'(X_n). \tag{7.13}$$

The mode coefficients a_{ij} are,

$$a_{ij} = e_{ij} \sqrt{\lambda_j N}. \tag{7.14}$$

The POD modes form an orthonormal set and are normalized such that,

$$\boldsymbol{\phi}_i \cdot \boldsymbol{\phi}_j = \delta_{ij}, \tag{7.15}$$

where δ_{ij} is the Kronecker delta and '$\cdot$' denotes the vector dot product. The eigenvalues have special significance because,

$$E_{tot} = \sum_{n=1}^{M} \overline{R(X_n, X_n)} = \sum_{j=1}^{N} \lambda_j. \tag{7.16}$$

Consequently, each eigenvalue represents the contribution of its corresponding mode to the total energy, and in the discussion of results, the energies (λ_j), will be normalized by this E_{tot}.

It should be noted that in the preceding formulation, thermodynamic variables are not considered because none were measured in these experiments. Sirovich (1987) and Rowley, Colonius & Murray (2004) state that in a compressible flow, both the velocity and thermodynamic variables are dynamically important and should be included in the analysis. In this work, only the streamwise-velocity fluctuations are measured and so the analysis is limited in this sense. However, researchers have

https://doi.org/10.1017/jfm.2018.1029 Published online by Cambridge University Press

used POD of single components of velocity to successfully examine the structure of compressible turbulent flows. For example, Murray *et al.* (2009) used the vertical component of velocity to study the structure of subsonic open cavities. To estimate the effect of a compressible flow field to a first approximation, the density field is broken into pre- and post-shock values. The first value is the value in the free stream and the second is calculated from the oblique shock relations with the shock position serving as a demarcation line. Then, POD analysis is carried out for $\sqrt{\rho}u'$ (instead of u'), which results in eigenvalues that are representative of $\rho u'^2$, which is the turbulent kinetic energy. However, we observed that this correction did not significantly alter the structure and spectrum of the POD modes for these experiments; hence, the formulation without the density was used.

8. Eigenvalues of snapshot POD analysis

In this section, we present and discuss the eigenvalue results from applying the snapshot POD method to the KTV data reported in earlier sections. In figure 15(*a*), we present the cumulative fractional energy versus mode number. For each case, the first mode accounts for ≈20–30 % of the E_{tot} (7.16) and the first 6–10 modes capture approximately 60 % of the E_{tot} in the flow. No clear trends as to the fraction of energy of the first mode or the cumulative fractional energy can be found between the different flow fields investigated in this work.

The eigenvalue spectrum is plotted for each case in figure 15(*b*). Knight & Sirovich (1990) and Moser (1994) suggest that the POD eigenfunctions are a good set of basis functions with which to form an inertial-range spectrum for inhomogeneous, turbulent flows, as is the case here. The famous inertial-range scaling due to Kolmogorov (Kolmogorov 1941) is

$$E \propto \epsilon^{2/3} k^{-5/3}, \tag{8.1}$$

where E is the energy per scalar wavenumber, ϵ is the dissipation rate and k is the wavenumber. Stated equivalently

$$\mathcal{E} \propto \epsilon^{2/3} k^{-11/3}, \tag{8.2}$$

where $\mathcal{E}$ is the energy per vector wavenumber. Knight & Sirovich (1990) argue that the wavenumber is proportional to the mode number as $k \propto j^{1/3}$, and so in the inertial range the eigenvalues scale as

$$\lambda_j \propto j^{-11/9}, \tag{8.3}$$

which is represented in figure 15(*b*) as a dashed line. Knight & Sirovich (1990) also state that the inertial range will be shorter by a factor of three in equivalent wavenumber space (measured in decades). The differences between the different spectra presented here are modest for mode numbers $j < 100$, above which the noise from the measurement technique may play a role.

The authors initially expected an appreciably different eigenvalue spectrum when comparing each case because of how dissimilar and inhomogeneous the flow fields are. For example, the 32° corner flow is inhomogeneous in the streamwise and wall-normal directions and has a relatively large separated region. This is in contrast to the boundary-layer flow, which is attached and inhomogeneous in only the wall-normal direction, yet the spectra are similar. However, upon close inspection, the first few POD modes do not clearly scale as $j^{-11/9}$, and these modes contain the structures (inhomogeneity and separation) which strongly modify the mean flow; this will be evident in the forthcoming presentation of the POD modes.

https://doi.org/10.1017/jfm.2018.1029 Published online by Cambridge University Press

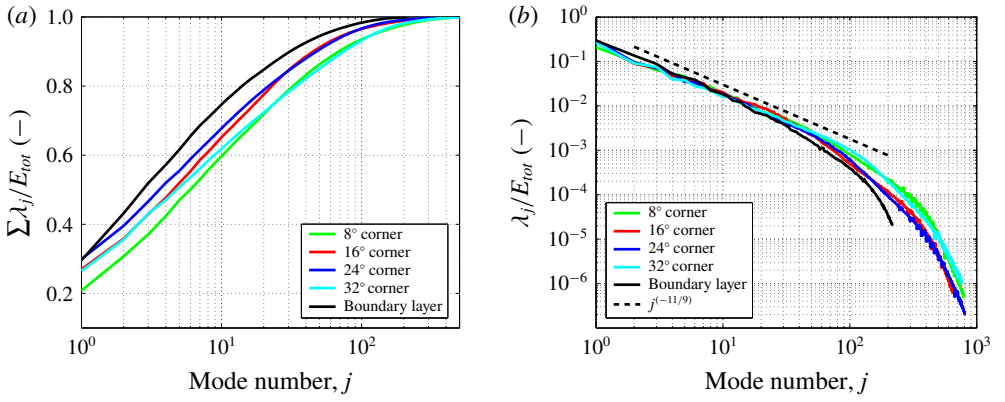


FIGURE 15. (Colour online) (*a*) The cumulative fraction of energy, $\sum \lambda_j/E_{tot}$. (*b*) The fraction of energy of each mode, λ_j/E_{tot}. The black line is the mode number raised to the $(-11/9)$ power as suggested by Knight & Sirovitch (Knight & Sirovich 1990).

This scaling of the eigenvalues is similar to that found in Piponniau *et al.* (2012) where a POD analysis was performed on PIV results from an induced-shock-wave/turbulent boundary-layer interaction. Piponniau *et al.* (2012) report a smaller observed value of the roll off ($\lambda \propto j^{-0.9}$) which may be due to the fact that: (i) the flow field is not the same (impinged-shock/boundary-layer interaction versus corner flow); (ii) it is understood that the wall-normal component of the fluctuating velocity tends to have a flatter spectrum in high-speed wall-bounded boundary layers than does the streamwise component (Brooks *et al.* 2016) and Piponniau *et al.* (2012) utilized both streamwise and wall-normal velocities in their analysis versus only streamwise in the present analysis; and (iii) the measurement technique was PIV in Piponniau *et al.* (2012) versus KTV in the present work.

9. POD coefficients and modes of 24-degree corner flow

Here, we will discuss the 24° corner flow case in detail because it is often explored in other literature. In figure 16(*a*), we present the first POD mode coefficients ($a_{i1}/\sqrt{E_{tot}}$) for the 24° corner flow. We do not observe any clear trends in time for this or any POD mode. Additionally, we do not observe any clear phenomena when constructing phase portraits (two different POD mode coefficients plotted against one another), or transforming the POD mode coefficients into frequency space. One reason for not observing any interesting phenomena, such as the low-frequency dynamics discussed in Clemens & Narayanaswamy (2014), is a lack of temporal resolution. The laser repetition rate for this experiment is fixed to 10 Hz dictating a Nyquist frequency of 5 Hz, which is far slower than the characteristic time scales of this flow.

The sample distribution of energy for the first POD mode of the 24° corner flow is presented in figure 16(*b*). There are no observable biases about the mean to within experimental error. Also in this figure, we mark the locations corresponding to 1.5 standard deviations (1.5σ) of the $|a_{i1}|$ samples which have the largest magnitude; we will use the samples that correspond to these large coefficient values (positive and negative) to gain insight into the mean-flow behaviour exhibited by the POD modes.

The first six POD modes for the 24° corner flow are shown as contours of ϕ_j in figure 17(*a*). To illustrate the effect of the different POD modes on the mean flow,

https://doi.org/10.1017/jfm.2018.1029 Published online by Cambridge University Press

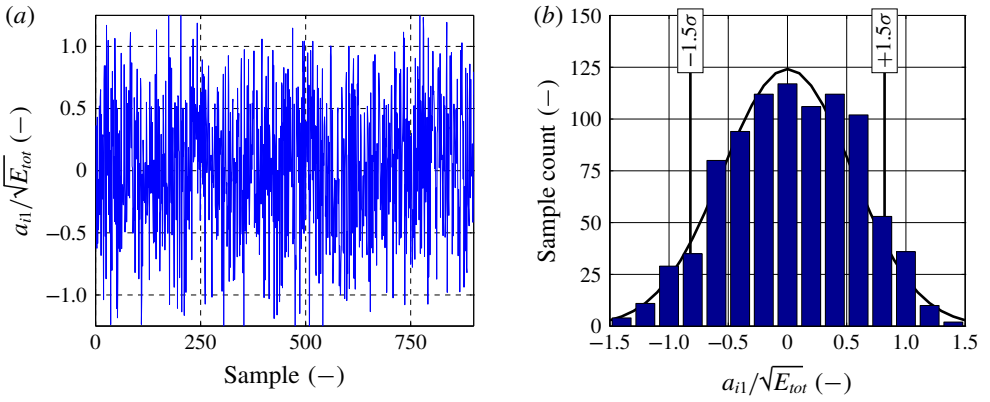


FIGURE 16. (Colour online) First POD mode coefficients for 24° corner flow. (*a*) Coefficients for POD mode $j = 1$, a_{i1} versus sample number. (*b*) Sample distribution of coefficients for mode $j = 1$. Vertical black bars mark 1.5 standard deviations (1.5σ) indicating large magnitude coefficients $|a_{i1}|$.

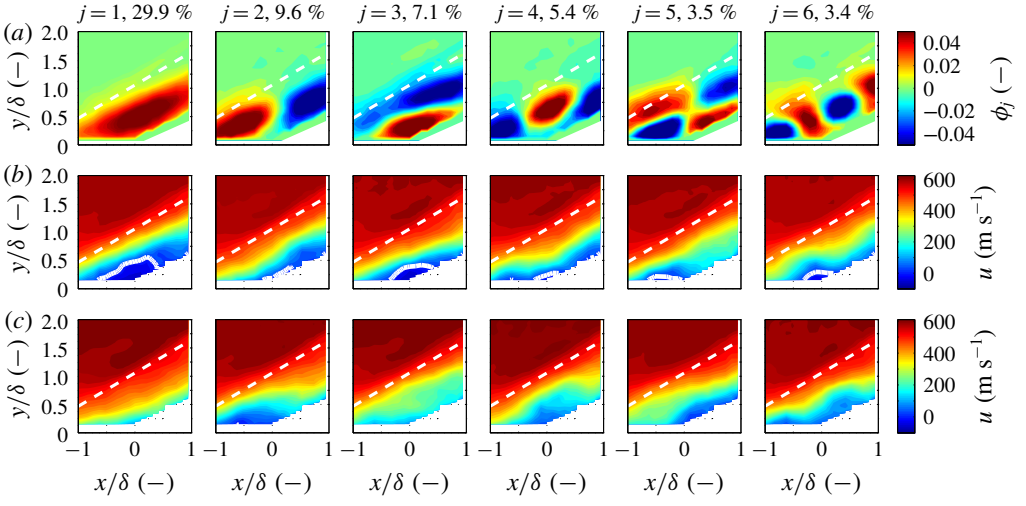


FIGURE 17. (Colour online) Snapshot POD analysis for the 24° corner flow. Each column corresponds to one of the first six POD modes marked by the mode number j and the fraction of energy associated with each mode in %. (*a*) POD modes for the 24° corner flow are shown as contours of ϕ_j. (*b*) The mean streamwise velocity of snapshots with the largest positive mode coefficients (samples falling to right of $+1.5\sigma$ in in figure 16). (*c*) The mean streamwise velocity of snapshots with the largest negative mode coefficients (samples falling to left of -1.5σ in in figure 16). A solid white line denotes the boundary between positive and negative streamwise velocity. A dashed white line denotes the mean shock location.

the mean streamwise velocity of snapshots that correspond to the largest positive and negative mode coefficients is presented in figures 17(*b*) and 17(*c*) respectively. That is, in figure 17(*b*), we present the mean of the streamwise velocity of the snapshots corresponding to samples falling above 1.5 standard deviations of the POD mode

https://doi.org/10.1017/jfm.2018.1029 Published online by Cambridge University Press

coefficient distribution ($+1.5\sigma$ of a_{i1}). And, in figure 17(*c*), we present the mean of the streamwise velocity of the snapshots corresponding to samples falling below 1.5 standard deviations of the POD mode coefficient distribution (-1.5σ of a_{i1}).

The first POD mode, ϕ_1, of the 24° corner flow case appears in the first row of the first column in figure 17. Inspecting the mean-velocity field associated with large values of the mode coefficients, it appears that this POD mode is associated with large-scale filling ($+1.5\sigma$ of a_{i1}, second row, first column of figure 17) and complete collapse (-1.5σ of a_{i1}, third row, first column of figure 17) of the separation bubble at the root of the corner. The second POD mode, (ϕ_2, second column of first row) appears to be the separation bubble oscillating in the streamwise direction as evidenced by the POD mode and the associated mean velocity fields associated with the large mode coefficients ($\pm 1.5\sigma$ of a_{i2}). It appears that there is a sloshing, or shift in the streamwise direction of high and low momentum fluid. The third POD mode (ϕ_3, third column of first row) appears to be smaller-scale separation bubble filling and collapse in comparison with ϕ_1. There is an additional flow feature: when the flow is separated, there is a momentum surplus in the region immediately above the separation location and when the separation bubble is collapsed, there is a momentum deficit in the same region. This is potentially indicative of snapshots where the separation bubble is in the process of filling or collapsing. Modes ϕ_4 and ϕ_5 (fourth and fifth column of first row, respectively) appear to be harmonics of modes ϕ_2 and ϕ_3, respectively. Mode ϕ_6 (sixth column of first row, respectively) is difficult to interpret, but could be a harmonic of ϕ_4. Higher-order modes, not pictured here, indicate increasingly smaller structures within the boundary layer and shock layer. In some of the higher modes, there are thin structures which appear close to the mean shock location, but these structures are associated with POD modes containing less than 1 % of the TKE in the flow. That is, the energy associated with fluctuations from the mean shock location are small relative to the fluctuations associated with the dynamics of the separation bubble.

10. Comparison of POD analyses between cases

The POD analysis applied to the 24° corner case that was presented in figure 17 is also applied to the 8° corner, 16° corner, 32° corner and boundary-layer cases and presented in figures 19–22, respectively.

Several characteristics of the POD analyses are common among each of the cases. For all cases, the POD modes only register interesting content within the boundary layer and shock layer. This is a sensible result as the free-stream disturbances are small and incoherent relative to the disturbances within the shock and boundary layers. For mode number higher than approximately $j = 10$, the POD modes are difficult to distinguish from one case to another, besides the obvious change in boundary geometry. That is, the disturbances evident in the high-order POD modes appear quite similar between cases in terms of distribution, amplitude, and length scale. To illustrate this point, the 30th POD mode (ϕ_{30}) is presented in figure 18 for each of the cases. The qualitative observation of commonality of the higher POD modes is also evident in the spectra of the eigenvalues presented in figure 15(*b*). The initial thought was that the commonality of the higher-order modes was due to noise in the measurement technique, which is also common among all cases. However, the signal-to-noise ratio appears sufficient at high mode number (figure 18).

Several characteristics of the POD analyses are dissimilar between the cases. In contrast to the 16°, 24° and 32° corner cases, the first POD of the 8° corner does not

https://doi.org/10.1017/jfm.2018.1029 Published online by Cambridge University Press

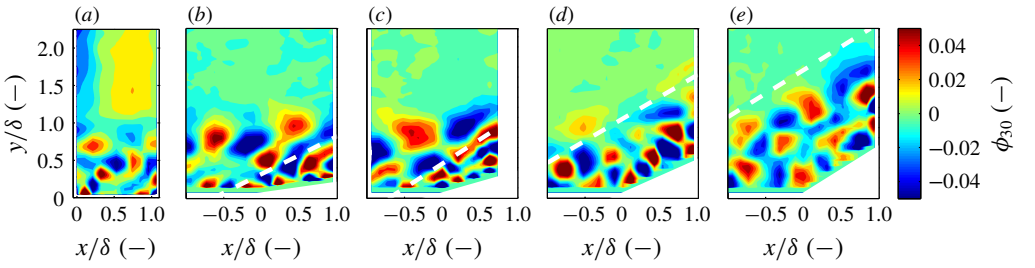


FIGURE 18. (Colour online) Comparison of the 30th POD mode (ϕ_{30}) among the boundary-layer and 8°, 16°, 24° and 32° corner flows, from left to right, respectively. A dashed white line denotes the mean shock location.

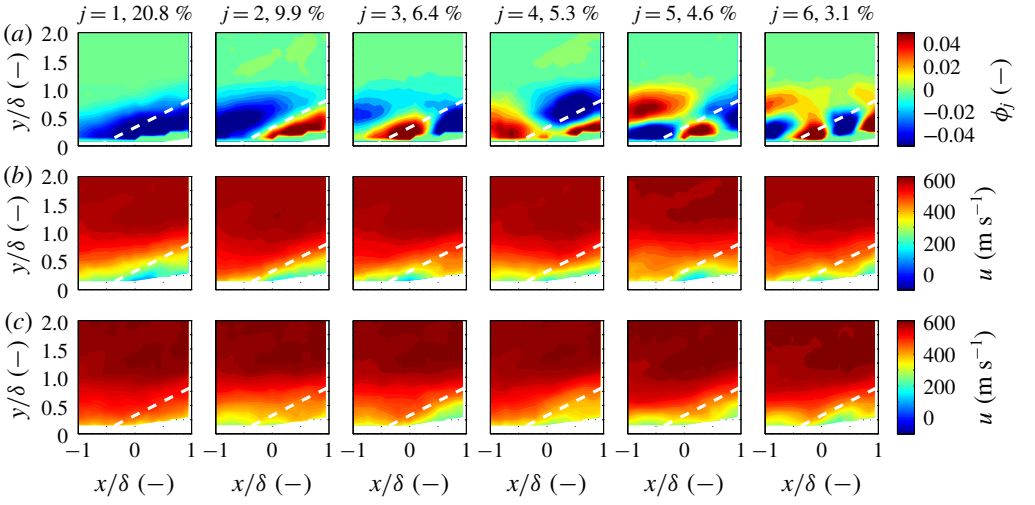


FIGURE 19. (Colour online) Snapshot POD analysis for the 8° corner flow. (*a*) POD modes are shown as contours of ϕ_j. (*b,c*) The mean streamwise velocity of snapshots that correspond to the largest positive and negative mode coefficients, respectively. A dashed white line denotes the mean shock location.

appear to indicate a relatively large separation bubble. Additionally, in the 24° and 32° cases, the shock wave appears to extend the upper boundary of where turbulent structures appear in the flow (figure 18*d,e*). This is juxtaposed to the 8° and 16° cases where this is not readily observed (figure 18*b,c*).

11. Conclusions

The incoming boundary layer and shock-wave/boundary-layer interactions over four compression corners at $M_\infty = 2.8$ were investigated using one-dimensional KTV in the M3CT. The focus of this study was the effect of compression-corner angle on streamwise turbulent kinetic energy (sTKE) and structure in Mach 2.8 flow. This canonical flow may be observed in practice as the deflection of a control surface on a vehicle in high-speed flight or in the flow path of a high-speed, air-breathing engine.

Typical Z-type schlieren images were recorded for each compression-corner flow to address concerns about potential tunnel-starting issues in the M3CT. We found no such

https://doi.org/10.1017/jfm.2018.1029 Published online by Cambridge University Press

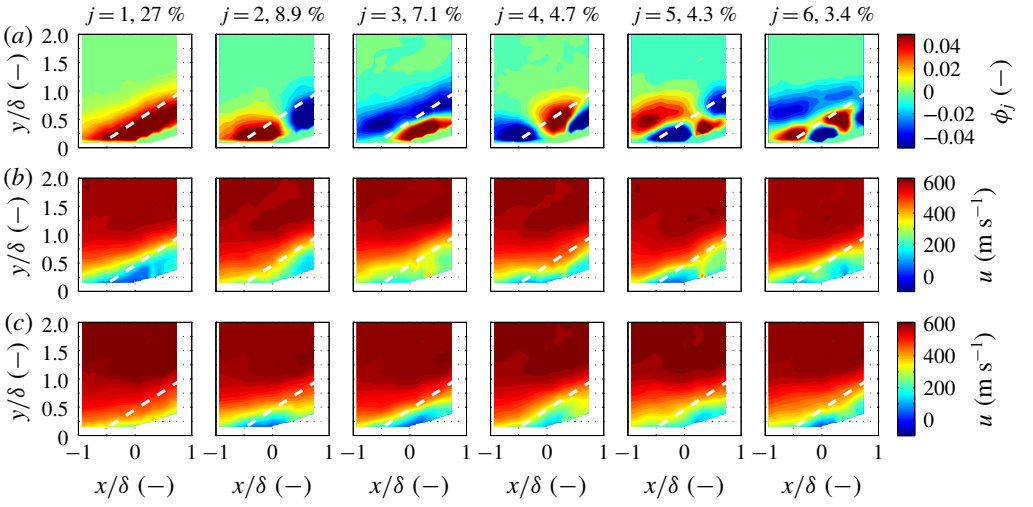


FIGURE 20. (Colour online) Snapshot POD analysis for the 16° corner flow. (*a*) POD modes are shown as contours of ϕ_j. (*b,c*) The mean streamwise velocity of snapshots that correspond to the largest positive and negative mode coefficients, respectively. A dashed white line denotes the mean shock location.

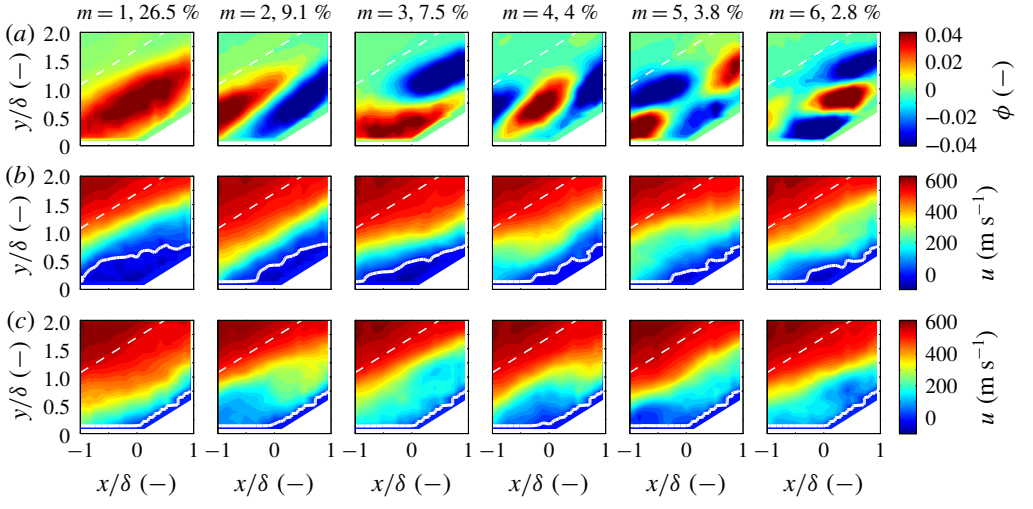


FIGURE 21. (Colour online) Snapshot POD analysis for the 32° corner flow. (*a*) POD modes are shown as contours of ϕ_j. (*b,c*) The mean streamwise velocity of snapshots that correspond to the largest positive and negative mode coefficients, respectively. A dashed white line denotes the mean shock location.

tunnel starting issues and made fits to the mean initial shock-wave angle. These data agreed with data in the literature, which built confidence in studying these geometries in the M3CT.

For the incoming boundary layer, data from ten mean- and fluctuating-velocity profiles spanning ≈11 mm or $x/\delta \approx 1.1$ in the streamwise direction were reduced and compared to data from the literature. These comparisons included van Direst I

https://doi.org/10.1017/jfm.2018.1029 Published online by Cambridge University Press

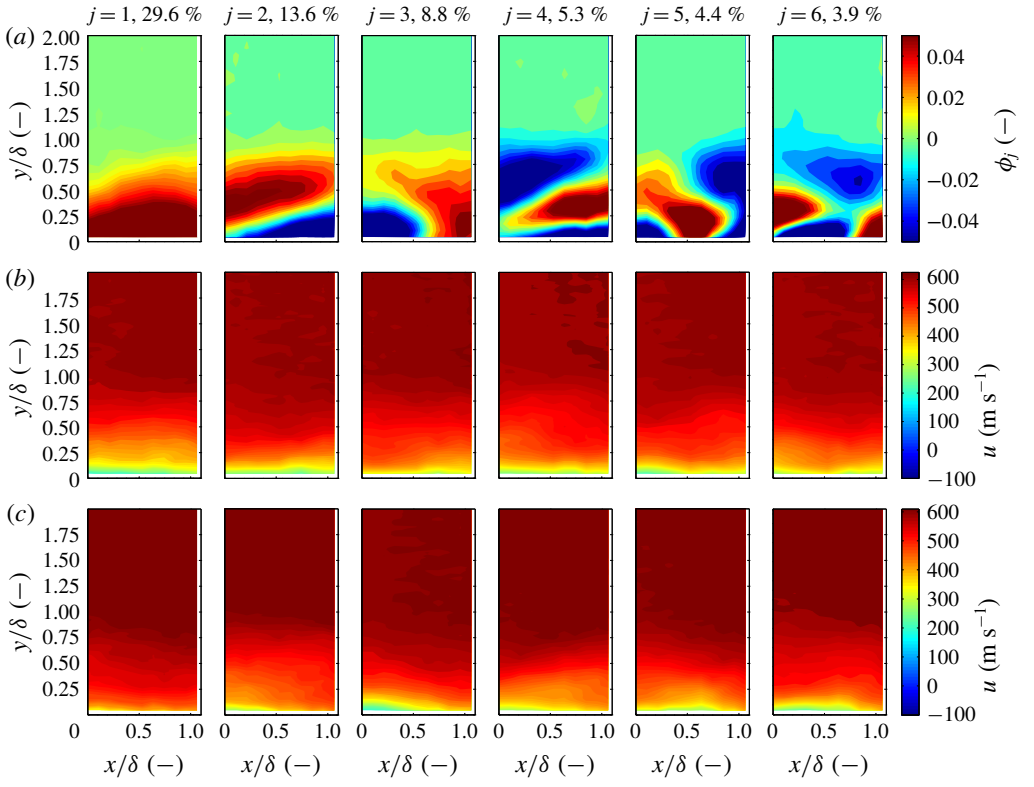


FIGURE 22. (Colour online) Snapshot POD analysis for the boundary-layer flow. Each column corresponds to one of the first six POD modes marked by the mode number j and the fraction of energy associated with each mode in per cent. (*a*) POD modes are shown as contours of ϕ_j. (*b,c*) The mean streamwise velocity of snapshots that correspond to the largest positive and negative mode coefficients, respectively.

scaling, Morkovin scaling of the streamwise-velocity fluctuations and longitudinal correlations. Comparisons are favourable between the KTV data collected in this work and experimental and computational data from the literature. From this, we concluded that the incoming flow could be nominally treated as a canonical supersonic, turbulent boundary layer and investigations of shock-wave/turbulent boundary-layer interactions could commence.

For the shock-wave/turbulent boundary-layer interactions, data from $\approx$20 mean- and fluctuating-velocity profiles spanning $\approx$22 mm or $x/\delta \approx 2.1$ were recorded for compression-corner angles of 8°, 16°, 24° and 32°. This was an effective demonstration of extending the application of tagging velocimetry into a complex flow field.

For the 16°, 24° and 32° cases, the shear layer near the root of interaction region was identified by fitting a coordinate system to the maxima of sTKE ($u'^2_{rms}/(U_2^2)$). To a first approximation, we observed the shear-layer profiles were self-similar by using the streamwise fluctuations in the laboratory frame as a surrogate for streamwise fluctuations in the shear-layer frame, which was the approach in Helm *et al.* (2014).

In an effort to identify trends of longitudinal turbulent stress with compression-corner angle, we defined a figure of merit termed the wall-normal integrated sTKE,

https://doi.org/10.1017/jfm.2018.1029 Published online by Cambridge University Press

$\overline{\text{sTKE}}$. This figure of merit is intended to identify the overall longitudinal turbulent stress contained in the flow at different x/δ locations, which should be relatively easy to compare between other experimental and computational studies. Because $\overline{\text{sTKE}}$ is the wall-normal integrated value, it will capture the amplitude of $u'^2_{rms}/(2U^2_\infty)$, in addition to the effect of the width of the shear layer in each case. We observe that the wall-normal integrated sTKE ($\overline{\text{sTKE}}$) scales as an exponential with respect to the compression-corner angle.

Proper orthogonal decomposition (POD) of the streamwise-velocity data was used to examine the structures and spectra in the flow. Knight & Sirovich (1990) and Moser (1994) suggest that the POD eigenfunctions are a good set of basis functions with which to form an inertial-range spectrum for inhomogeneous, turbulent flows and such a spectrum was identified in this work. That is, we found the POD eigenspectra to scale as $\lambda_j \propto j^{-11/9}$ which is analogous to the famous inertial-range scaling due to Kolmogorov (Kolmogorov 1941) ($E \propto \epsilon^{2/3}k^{-5/3}$). At a POD mode number greater than ≈ 10 there was an initially unanticipated similarity between the eigenspectra considering how dissimilar and inhomogeneous each case is (e.g. the boundary-layer flow versus the 32° corner flow). However, upon close inspection, the first few POD modes do not clearly scale as $j^{-11/9}$, and these modes contain the structures (inhomogeneity and separation) which strongly modify the mean flow. Following the first $\approx$10 modes, the similarity of the inertial range is apparent between each case.

To identify the modification of the mean flow due to each POD mode, we presented the mean streamwise velocity of the samples which correspond to the POD mode coefficients falling above and below 1.5 standard deviations ($\pm 1.5\sigma$ of a_{ij}). We observed that the first several modes are somewhat similar between each compression-corner case (with the exception of the 8° corner where the flow was mostly attached). These first POD modes contain most of the kinetic energy and are those that modify the mean flow, giving rise to features such as separation bubble filling/collapse and oscillation.

Acknowledgements

The M3CT facilities were supplied by the Arnold Engineering Development Complex (AEDC). The Air Force Summer Faculty Fellowship Program (SFFP) supported M.A.M. and N.J.P. with a stipend for this work. M.A.M. and N.J.P. were supported by AFOSR Young Investigator Program Grant FA9550-16-1-0262 and equipment for this work was supported by AFOSR DURIP Grant FA9550-15-1-0325; I. Leyva of AFOSR is the Program Manager for both grants. We acknowledge the machine work done by M. Simonovic and M. Reid of the Stevens Institute of Technology. We also would like to thank J. Brooks of the University of Maryland for assistance with operating the wind tunnel and the Pitot measurements. We would like to acknowledge the encouragement of J. Laffery and D. Marren of AEDC White Oak. Finally, we would like to acknowledge the reviewers for providing valuable insight into this work.

Supplementary movie

Supplementary movies are available at https://doi.org/10.1017/jfm.2018.1029.

https://doi.org/10.1017/jfm.2018.1029 Published online by Cambridge University Press

REFERENCES

ADAMS, N. A. 2000 Direct simulation of the turbulent boundary layer along a compression ramp at $m = 3$ and $\mathrm{re}_\Theta = 1685$. *J. Fluid Mech.* **420**, 47–83.

ANDRÉ, M. A., BARDET, P. M., BURNS, R. A. & DANEHY, P. M. 2017 Characterization of hydroxyl tagging velocimetry for low-speed flows. *Meas. Sci. Technol.* **28** (8), 085202.

ANDRÉ, M. A., BURNS, R. A., DANEHY, P. M., CADELL, S. R., WOODS, B. G. & BARDET, P. M. 2018 Development of N_2O-MTV for low-speed flow and in-situ deployment to an integral effect test facility. *Exp. Fluids* **59** (1), 14.

BABINSKY, H. & HARVEY, J. K. (Eds) 2011 *Shock Wave-Boundary-Layer Interactions*, 1st edn. Cambridge University Press.

BALLA, R. J. 2013 Iodine tagging velocimetry in a Mach 10 wake. *AIAA J.* **51** (7), 1–3.

BALLA, R. J. & EVERHART, J. L. 2012 Rayleigh scattering density measurements, cluster theory, and nucleation calculations at Mach 10. *AIAA J.* **50** (3), 698–707.

BARKER, P., BISHOP, A. & RUBINSZTEIN-DUNLOP, H. 1997 Supersonic velocimetry in a shock tube using laser enhanced ionisation and planar laser induced fluorescence. *Appl. Phys.* B **64** (3), 369–376.

BATHEL, B. F., DANEHY, P. M., INMAN, J. A., JONES, S. B., IVEY, C. B. & GOYNE, C. P. 2011 Velocity profile measurements in hypersonic flows using sequentially imaged fluorescence-based molecular tagging. *AIAA J.* **49** (9), 1883–1896.

BERKOOZ, G., HOLMES, P. & LUMLEY, J. L. 1993 The proper orthogonal decomposition in the analysis of turbulent flows. *Annu. Rev. Fluid Mech.* **25** (1), 539–575.

BOEDEKER, L. R. 1989 Velocity measurement by H_2O photolysis and laser-induced fluorescence of OH. *Opt. Lett.* **14** (10), 473–475.

BONNET, J. P., COLE, D. R., DELVILLE, J., GLAUSER, M. N. & UKEILEY, L. S. 1994 Stochastic estimation and proper orthogonal decomposition: complementary techniques for identifying structure. *Exp. Fluids* **17** (5), 307–314.

BRADSHAW, P. 1977 Compressible turbulent shear layers. *Annu. Rev. Fluid Mech.* **9** (1), 33–52.

BROOKS, J., GUPTA, A., SMITH, M. S. & MARINEAU, E. C. 2014 Development of non-intrusive velocity measurement capabilities at AEDC tunnel 9. In *Proceedings of 52nd Aerospace Sciences Meeting, SciTech. National Harbor, Maryland*. AIAA-2014-1239.

BROOKS, J. M., GUPTA, A. K., SMITH, M. S. & MARINEAU, E. C. 2015 Development of particle image velocimetry in a Mach 2.7 wind tunnel at AEDC White Oak. In *Proceedings of 53nd Aerospace Sciences Meeting, SciTech. Kissimmee, Florida*. AIAA-2015-1915.

BROOKS, J. M., GUPTA, A. K., SMITH, M. S. & MARINEAU, E. C. 2016 PIV measurements of Mach 2.7 turbulent boundary layer with varying Reynolds numbers. In *Proceedings of 54th Aerospace Sciences Meeting, SciTech. San Diego, California*. AIAA-2016-1147.

BROOKS, J. M., GUPTA, A. K., SMITH, M. S. & MARINEAU, E. C. 2018 Particle image velocimetry measurements of Mach 3 turbulent boundary layers at low Reynolds numbers. *Exp. Fluids* **59** (3), 83.

CHANG, R. S. F., HORIGUCHI, H. & SETSER, D. W. 1980 Radiative lifetimes and twobody collisional deactivation rate constants in argon for $Kr(4p^55p)$ and $Kr(4p^55p)$ states. *J. Chem. Phys.* **73** (2), 778–790.

CHEN, H., REUSS, D. L., HUNG, D. L. S. & SICK, V. 2013 A practical guide for using proper orthogonal decomposition in engine research. *Intl J. Engine Res.* **14** (4), 307–319.

CHEN, H., REUSS, D. L. & SICK, V. 2012 On the use and interpretation of proper orthogonal decomposition of in-cylinder engine flows. *Meas. Sci. Technol.* **23** (8), 085302.

CLEMENS, N. T. & NARAYANASWAMY, V. 2014 Low-frequency unsteadiness of shock wave/turbulent boundary layer interactions. *Annu. Rev. Fluid Mech.* **46**, 469–492.

DAM, N., KLEIN-DOUWEL, R. J. H., SIJTSEMA, N. M. & TER MEULEN, J. J. 2001 Nitric oxide flow tagging in unseeded air. *Opt. Lett.* **26** (1), 36–38.

DOLLING, D. S. 2001 Fifty years of shock-wave/boundary-layer interaction research: What next?. *AIAA J.* **39** (8), 1517–1531.

DRUAULT, P., GUIBERT, P. & ALIZON, F. 2005 Use of proper orthogonal decomposition for time interpolation from PIV data. *Exp. Fluids* **39** (6), 1009–1023.

https://doi.org/10.1017/jfm.2018.1029 Published online by Cambridge University Press

DUAN, L, BEEKMAN, I & MARTIN, M. P. 2011 Direct numerical simulation of hypersonic turbulent boundary layers. Part 3. Effect of Mach number. *J. Fluid Mech.* **672**, 245–267.

EDWARDS, M. R., DOGARIU, A. & MILES, R. B. 2015 Simultaneous temperature and velocity measurements in air with femtosecond laser tagging. *AIAA J.* **53** (8), 2280–2288.

ELENA, M., LACHARME, J. P. & GAVIGLIO, J. 1985 Comparison of hot-wire and laser Doppler anemometry methods in supersonic turbulent boundary layers. In *Proceedings of 2nd International Symposium on Laser Anemometry*, pp. 151–157.

GAITONDE, D. V. 2015 Progress in shock wave/boundary layer interactions. *Prog. Aerosp. Sci.* **72**, 80–99.

GENDRICH, C. P. & KOOCHESFAHANI, M. M. 1996 A spatial correlation technique for estimating velocity fields using molecular tagging velocimetry (MTV). *Exp. Fluids* **22** (1), 67–77.

GENDRICH, C. P., KOOCHESFAHANI, M. M. & NOCERA, D. G. 1997 Molecular tagging velocimetry and other novel applications of a new phosphorescent supramolecule. *Exp. Fluids* **23** (5), 361–372.

GIEPMAN, R. H. M., SCHRIJER, F. F. J. & VAN OUDHEUSDEN, B. W. 2015 High-resolution PIV measurements of a transitional shock wave-boundary layer interaction. *Exp. Fluids* **56** (6), 113.

HAERTIG, J., HAVERMANN, M., REY, C. & GEORGE, A. 2002 Particle image velocimetry in Mach 3.5 and 4.5 shock-tunnel flows. *AIAA J.* **40** (6), 1056–1060.

HANDA, T., MII, K., SAKURAI, T., IMAMURA, K., MIZUTA, S. & ANDO, Y. 2014 Study on supersonic rectangular microjets using molecular tagging velocimetry. *Exp. Fluids* **55** (5), 1–9.

HELM, C., MARTIN, M. P. & DUPONT, P. 2014 Characterization of the shear layer in a Mach 3 shock/turbulent boundary layer interaction. *J Phys.: Conf. Ser.* **506** (1), 012013.

HILL, R. B. & KLEWICKI, J. C. 1996 Data reduction methods for flow tagging velocity measurements. *Exp. Fluids* **20** (3), 142–152.

HILLER, B., BOOMAN, R. A., HASSA, C. & HANSON, R. K. 1984 Velocity visualization in gas flows using laser-induced phosphorescence of biacetyl. *Rev. Sci. Instrum.* **55** (12), 1964–1967.

HSU, A. G., SRINIVASAN, R., BOWERSOX, R. D. W. & NORTH, S. W. 2009*a* Molecular tagging using vibrationally excited nitric oxide in an underexpanded jet flowfield. *AIAA J.* **47** (11), 2597–2604.

HSU, A. G., SRINIVASAN, R., BOWERSOX, R. D. W. & NORTH, S. W. 2009*b* Two-component molecular tagging velocimetry utilizing NO fluorescence lifetime and NO_2 photodissociation techniques in an underexpanded jet flowfield. *Appl. Opt.* **48** (22), 4414–4423.

HUANG, P. G. & COLEMAN, G. N. 1994 Van driest transformation and compressible wall-bounded flows. *AIAA J.* **32** (10), 2110–2113.

HUMBLE, R. A., ELSINGA, G. E., SCARANO, F. & VAN OUDHEUSDEN, B. W. 2009 Three-dimensional instantaneous structure of a shock wave/turbulent boundary layer interaction. *J. Fluid Mech.* **622**, 33–62.

HUMBLE, R. A., SCARANO, F. & VAN OUDHEUSDEN, B. W. 2007 Particle image velocimetry measurements of a shock wave/turbulent boundary layer interaction. *Exp. Fluids* **43** (2–3), 173–183.

JIANG, N., HALLS, B. R., STAUFFER, H. U., DANEHY, P. M., GORD, J. R. & ROY, S. 2016 Selective two-photon absorptive resonance femtosecond-laser electronic-excitation tagging velocimetry. *Opt. Lett.* **41** (10), 2225–2228.

JIANG, N., MANCE, J. G., SLIPCHENKO, M. N., FELVER, J. J., STAUFFER, H. U., YI, T., DANEHY, P. M. & ROY, S. 2017 Seedless velocimetry at 100 kHz with picosecond-laser electronic-excitation tagging. *Opt. Lett.* **42** (2), 239–242.

JOHN, B., KULKARNI, V. N. & NATARAJAN, G. 2014 Shock wave boundary layer interactions in hypersonic flows. *Intl J. Heat Mass Transfer* **70**, 81–90.

VON KÁRMÁN, T. 1934 Turbulence and skin friction. *J. Aeronaut. Sci.* **1** (1), 1–20.

KLEBANOFF, P. S. 1955 Characteristics of turbulence in a boundary layer with zero pressure gradient. *NACA TR*-1247.

https://doi.org/10.1017/jfm.2018.1029 Published online by Cambridge University Press

KNIGHT, B. & SIROVICH, L. 1990 Kolmogorov inertial range for inhomogeneous turbulent flows. *Phys. Rev. Lett.* **65** (11), 1356–1359.

KNIGHT, D., YAN, H., PANARAS, A. G. & ZHELTOVODOV, A. 2003 Advances in CFD prediction of shock wave turbulent boundary layer interactions. *Prog. Aerosp. Sci.* **39** (2), 121–184.

KOLMOGOROV, A. N. 1941 The local structure of turbulence in incompressible viscous fluid for very large Reynolds numbers. *Proc. R. Soc. Lond.* A **30** (4), 299–303.

LEMPERT, W. R., BOEHM, M., JIANG, N., GIMELSHEIN, S. & LEVIN, D. 2003 Comparison of molecular tagging velocimetry data and direct simulation Monte Carlo simulations in supersonic micro jet flows. *Exp. Fluids* **34** (3), 403–411.

LEMPERT, W. R., JIANG, N., SETHURAM, S. & SAMIMY, M. 2002 Molecular tagging velocimetry measurements in supersonic microjets. *AIAA J.* **40** (6), 1065–1070.

LOTH, E. 2008 Compressibility and rarefaction effects on drag of a spherical particle. *AIAA J.* **46** (9), 2219–2228.

LUMLEY, J. L. 1967 The structure of inhomogeneous turbulent flows. In *Atmospheric Turbulence and Radio Wave Propagation* (ed. A. M. Yaglom & V. I. Tatarsky), pp. 166–176. Nauka Press.

MARTIN, M. P. 2007 Direct numerical simulation of hypersonic turbulent boundary layers. Part 1. Initialization and comparison with experiments. *J. Fluid Mech.* **570**, 347–364.

MCDANIEL, J. C., HILLER, B. & HANSON, R. K. 1983 Simultaneous multiple-point velocity measurements using laser-induced iodine fluorescence. *Opt. Lett.* **8** (1), 51–53.

MICHAEL, J. B., EDWARDS, M. R., DOGARIU, A. & MILES, R. B. 2011 Femtosecond laser electronic excitation tagging for quantitative velocity imaging in air. *Appl. Opt.* **50** (26), 5158–5162.

MILES, R., COHEN, C., CONNORS, J., HOWARD, P., HUANG, S., MARKOVITZ, E. & RUSSELL, G. 1987 Velocity measurements by vibrational tagging and fluorescent probing of oxygen. *Opt. Lett.* **12** (11), 861–863.

MILES, R. B., CONNORS, J. J., MARKOVITZ, E. C., HOWARD, P. J. & ROTH, G. J. 1989 Instantaneous profiles and turbulence statistics of supersonic free shear layers by Raman excitation plus laser-induced electronic fluorescence (RELIEF) velocity tagging of oxygen. *Exp. Fluids* **8** (1–2), 17–24.

MILES, R. B., GRINSTEAD, J., KOHL, R. H. & DISKIN, G. 2000 The RELIEF flow tagging technique and its application in engine testing facilities and for helium-air mixing studies. *Meas. Sci. Technol.* **11** (9), 1272–1281.

MILES, R. B. & LEMPERT, W. R. 1997 Quantitative flow visualization in unseeded flows. *Annu. Rev. Fluid Mech.* **29** (1), 285–326.

MILES, R. B., ZHOU, D., ZHANG, B. & LEMPERT, W. R. 1993 Fundamental turbulence measurements by RELIEF flow tagging. *AIAA J.* **31** (3), 447–452.

MILLS, J. L. 2016 Investigation of multi-photon excitation in argon with applications in hypersonic flow diagnostics. PhD thesis, Old Dominion University.

MILLS, J. L., SUKENIK, C. I. & BALLA, R. J. 2011 Hypersonic wake diagnostics using laser induced fluorescence techniques. In *Proceedings of 42nd AIAA Plasmadynamics and Lasers Conference, Honolulu, Hawaii*. AIAA 2011-3459.

MORKOVIN, M. V. 1962 Effects of compressibility on turbulent flows. In *Mécanique de la Turbulence*, pp. 367–380. CNRS.

MOSER, R. D. 1994 Kolmogorov inertial range spectra for inhomogeneous turbulence. *Phys. Fluids* **6** (2), 794–801.

MURRAY, N., SÄLLSTRÖM, E. & UKEILEY, L. 2009 Properties of subsonic open cavity flow fields. *Phys. Fluids* **21** (9), 095103.

MUSTAFA, M. A., HUNT, M. B., PARZIALE, N. J., SMITH, M. S. & MARINEAU, E. C. 2017*a* Krypton tagging velocimetry (KTV) investigation of shock-wave/turbulent boundary-layer interaction. In *Proceedings of AIAA SciTech 2017. Grapevine, Texas*. AIAA-2017-0025.

MUSTAFA, M. A. & PARZIALE, N. J. 2017 Krypton tagging velocimetry in the stevens shock tube. In *Proceedings of 33rd AIAA Aerodynamic Measurement Technology and Ground Testing Conference. Denver, Colorado*. AIAA-2017-3897.

https://doi.org/10.1017/jfm.2018.1029 Published online by Cambridge University Press

MUSTAFA, M. A. & PARZIALE, N. J. 2018 Simplified read schemes for krypton tagging velocimetry in N_2 and air. *Opt. Lett.* **43** (12), 2909–2912.

MUSTAFA, M. A., PARZIALE, N. J., SMITH, M. S. & MARINEAU, E. C. 2017*b* Nonintrusive freestream velocity measurement in a large-scale hypersonic wind tunnel. *AIAA J.* **55** (10), 3611–3616.

MUSTAFA, M. A., PARZIALE, N. J., SMITH, M. S. & MARINEAU, E. C. 2018 Two-dimensional Krypton Tagging Velocimetry (KTV-2D) investigation of shock-wave/turbulent boundary-layer interaction. In *Proceedings of AIAA SciTech 2018. Kissimmee, Florida*. AIAA-2018-1771.

O'HAVER, T. 1997 *A Pragmatic Introduction to Signal Processing*. University of Maryland at College Park.

ORELLANO, A. & WENGLE, H. 2001 Pod analysis of coherent structures in forced turbulent flow over a fence. *J. Turbul.* **2**, N8.

PARZIALE, N. J., SMITH, M. S. & MARINEAU, E. C. 2015*a* Krypton tagging velocimetry for use in high-speed ground-test facilities. In *Proceedings of AIAA SciTech 2015. Kissimmee, Florida*. AIAA-2015-1484.

PARZIALE, N. J., SMITH, M. S. & MARINEAU, E. C. 2015*b* Krypton tagging velocimetry of an underexpanded jet. *Appl. Opt.* **54** (16), 5094–5101.

PIPONNIAU, S., COLLIN, E., DUPONT, P. & DEBIÈVE, J. 2012 Reconstruction of velocity fields from wall pressure measurements in a shock wave/turbulent boundary layer interaction. *Intl J. Heat Fluid Flow* **35**, 176–186.

PITZ, R. W., LAHR, M. D., DOUGLAS, Z. W., WEHRMEYER, J. A., HU, S., CARTER, C. D., HSU, K.-Y., LUM, C. & KOOCHESFAHANI, M. M. 2005 Hydroxyl tagging velocimetry in a supersonic flow over a cavity. *Appl. Opt.* **44** (31), 6692–6700.

PORTER, K. M. & POGGIE, J. 2017 Turbulent structure and large-scale unsteadiness in shock-wave/boundary layer interaction. In *Proceedings of AIAA SciTech 2017. Grapevine, Texas*. AIAA-2017-0533.

RIBAROV, L. A., WEHRMEYER, J. A., BATLIWALA, F., PITZ, R. W. & DEBARBER, P. A. 1999 Ozone tagging velocimetry using narrowband excimer lasers. *AIAA J.* **37** (6), 708–714.

ROWLEY, C. W., COLONIUS, T. & MURRAY, R. M. 2004 Model reduction for compressible flows using pod and galerkin projection. *Phys.* D **189** (1–2), 115–129.

SÁNCHEZ-GONZÁLEZ, R., BOWERSOX, R. D. W. & NORTH, S. W. 2012 Simultaneous velocity and temperature measurements in gaseous flowfields using the vibrationally excited nitric oxide monitoring technique: a comprehensive study. *Appl. Opt.* **51** (9), 1216–1228.

SÁNCHEZ-GONZÁLEZ, R., BOWERSOX, R. D. W. & NORTH, S. W. 2014 Vibrationally excited NO tagging by NO($A^2\Sigma^+$) fluorescence and quenching for simultaneous velocimetry and thermometry in gaseous flows. *Opt. Lett.* **39** (9), 2771–2774.

SÁNCHEZ-GONZÁLEZ, R., SRINIVASAN, R., BOWERSOX, R. D. W. & NORTH, S. W. 2011 Simultaneous velocity and temperature measurements in gaseous flow fields using the venom technique. *Opt. Lett.* **36** (2), 196–198.

SCHLICHTING, H. 2000 *Boundary-Layer Theory*. Springer.

SCHOENHERR, K. E. 1932 Resistance of flat surfaces moving through a fluid. *Trans. Soc. Nav. Archit. Mar. Engrs* **40**, 279–313.

SETTLES, G. S. 2001 *Schlieren and Shadowgraph Techniques*, 1st edn. Springer.

SETTLES, G. S. & DODSON, L. J. 1994 Hypersonic shock/boundary-layer interaction database: new and corrected data. *NASA CR* 177638.

SETTLES, G. S., FITZPATRICK, T. J. & BOGDONOFF, S. M. 1979 Detailed study of attached and separated compression corner flowfields in high Reynolds number supersonic flow. *AIAA J.* **17** (6), 579–585.

SETTLES, G. S., VAS, I. E. & BOGDONOFF, S. M. 1976 Details of a shock-separated turbulent boundary layer at a compression corner. *AIAA J.* **14** (12), 1709–1715.

SIJTSEMA, N. M., DAM, N. J., KLEIN-DOUWEL, R. J. H. & TER MEULEN, J. J. 2002 Air photolysis and recombination tracking: A new molecular tagging velocimetry scheme. *AIAA J.* **40** (6), 1061–1064.

https://doi.org/10.1017/jfm.2018.1029 Published online by Cambridge University Press

SIROVICH, L. 1987 Turbulence and the dynamics of coherent structures, Part I: coherent structures. *Q. Appl. Maths* **45** (3), 561–571.

SMITS, A. J. & MUCK, K.-C. 1987 Experimental study of three shock wave/turbulent boundary layer interactions. *J. Fluid Mech.* **182**, 291–314.

SPAID, F. W. & FRISHETT, J. C. 1972 Incipient separation of a supersonic, turbulent boundary layer, including effects of heat transfer. *AIAA* **10** (7), 915–922.

STIER, B. & KOOCHESFAHANI, M. M. 1999 Molecular tagging velocimetry (MTV) measurements in gas phase flows. *Exp. Fluids* **26** (4), 297–304.

STÖHR, M., SADANANDAN, R. & MEIER, W. 2011 Phase-resolved characterization of vortex–flame interaction in a turbulent swirl flame. *Exp. Fluids* **51** (4), 1153–1167.

TAIRA, K., BRUNTON, S. L., DAWSON, S. T. M., ROWLEY, C. W., COLONIUS, T., MCKEON, B. J., SCHMIDT, O. T., GORDEYEV, S., THEOFILIS, V. & UKEILEY, L. S. 2017 Modal analysis of fluid flows: an overview. *AIAA J.* **55** (12), 1–29.

TENNEKES, H. & LUMLEY, J. L. 1972 *A First Course in Turbulence*. MIT Press.

TU, J. H., ROWLEY, C. W., KUTZ, J. N. & SHANG, J. K. 2014 Spectral analysis of fluid flows using sub-Nyquist-rate PIV data. *Exp. Fluids* **55** (9), 1805.

VAN DER LAAN, W. P. N., TOLBOOM, R. A. L., DAM, N. J. & TER MEULEN, J. J. 2003 Molecular tagging velocimetry in the wake of an object in supersonic flow. *Exp. Fluids* **34** (4), 531–534.

WANG, B., SANDHAM, N. D., HU, Z. & LIU, W. 2015 Numerical study of oblique shock-wave/boundary-layer interaction considering sidewall effects. *J. Fluid Mech.* **767**, 526–561.

WEHRMEYER, J. A., RIBAROV, L. A., OGUSS, D. A. & PITZ, R. W. 1999 Flame flow tagging velocimetry with 193 nm H_2O photodissociation. *Appl. Opt.* **38** (33), 6912–6917.

WU, M. & MARTIN, M. P. 2007 Direct numerical simulation of supersonic turbulent boundary layer over a compression ramp. *AIAA J.* **45** (4), 879–889.

WU, M. & MARTIN, M. P. 2008 Analysis of shock motion in shockwave and turbulent boundary layer interaction using direct numerical simulation data. *J. Fluid Mech.* **594**, 71–83.

ZAHRADKA, D., PARZIALE, N. J., SMITH, M. S. & MARINEAU, E. C. 2016*a* Krypton tagging velocimetry in a turbulent Mach 2.7 boundary layer. *Exp. Fluids* **57**, 62.

ZAHRADKA, D., PARZIALE, N. J., SMITH, M. S. & MARINEAU, E. C. 2016*b* Krypton tagging velocimetry (KTV) in supersonic turbulent boundary layers. In *Proceedings of AIAA SciTech 2016. San Diego, California*. AIAA-2016-1587.

ZHANG, S., YU, X., YAN, H., HUANG, H. & LIU, H. 2017 Molecular tagging velocimetry of NH fluorescence in a high-enthalpy rarefied gas flow. *Appl. Phys.* B **123** (4), 122.

https://doi.org/10.1017/jfm.2018.1029 Published online by Cambridge University Press